Master Thesis

Micromechanical Characterization of Self-Organized $Ti_{1-x}Al_xN$ Nanolamellae: The Influence of Interface Coherency and Phase Alteration on Fracture Behaviour

Michael Meindlhumer

Department Materialphysik
Montanuniversität Leoben
Jahnstraße 12
8700 Leoben

May 2016

Affidavit

I declare, in lieu of oath, that I wrote this thesis and performed the associated research myself, using only literature cited in this volume.

Leoben, May 2016 Michael Meindlhumer

Eidesstaatliche Erklärung

Ich erkläre an Eides statt, dass ich diese Arbeit selbständig verfasst, andere als die angegebenen Quellen und Hilfsmittel nicht benutzt, und mich auch sonst keiner unerlaubten Hilfsmittel bedient habe.

Leoben, Mai 2016 Michael Meindlhumer

Abstract

Mechanical properties of nanostructured hard coatings depend primarily on coating phase, microstructure and residual stress state. Besides hardness, there is a strong effort to enhance fracture properties of the coatings, in particular fracture toughness and fracture stress.

In the case of monolithic ceramic coatings, the usually observed intergranular fracture originates from columnar grain morphology and results in brittle coating behaviour. Apart from nanostructured and multi-layered coatings, periodic phase alteration provides an opportunity to enhance fracture properties of brittle materials. Thereby the nacre of molluscs is a leading model of fracture toughness enhancement, originating from alternating hard mineral and soft protein sublayers.

In this work, mechanical properties of three different, self-organized nanostructured $Ti_{1-x}Al_xN$ coatings are investigated. The coatings, which were synthetized using chemical vapour deposition, possess a very unique microstructure which was formed as a result of self-organized growth. The microstructure was characterized using transmission electron microscopy and the phase composition is evaluated using X-ray diffraction. The microstructure of the first coating shows a cubic-wurtzite alteration of the Ti-rich and Al-rich nitride phases, whereas the second coating is composed completely of cubic phases. In the third sample the phases were altered leading to a multi-layered coating with both cubic-cubic and cubic-wurtzite phases.

Furthermore hardness and indentation modulus were characterized using nanoindentation. For all samples, Young's modulus, fracture stress and fracture toughness were determined by micro-cantilever bending experiments in a scanning electron microscope. These experiments were carried out for the in-plane as well as the out-of-plane bending force orientation.

The results reveal outstanding mechanical properties for all three coatings investigated. Hardness is in the range of 26–37 GPa. Fracture stress depends on the phase of the nanostructured coatings and reaches a maximum of 7.9 GPa for the multi-layered sample. The micromechanical bending experiments show nearly isotropic elastic response for the monolithic coatings whereas only a slight anisotropy was found in the case of the multi-layered sample. In the case of fracture toughness a complex dependence on the coating morphology is observed.

Moreover, both the in-situ analysis of the crack propagation in the multi-layered structures during the cantilever bending experiments as well as the ex-situ analysis of the fracture surfaces helps to improve our understanding of fracture behaviour of nanostructured coatings.

Kurzfassung

Mechanische Eigenschaften von nanostrukturierten, harten Beschichtungen hängen primär von der Phase der Beschichtung, der Mikrostruktur der Beschichtung und dem Eigenspannungszustand ab. Neben der Härte, werden auch große Anstrengungen unternommen die Brucheigenschaften der Beschichtungen, namentlich Bruchzähigkeit und Bruchspannung, zu verbessern.

Im Fall von monolithischen keramischen Beschichtungen, wird der normalerweise beobachtete intergranulare Bruch durch die kolumnare Kornmorphologie hervorgerufen. Sowohl nanostrukturierte und multilagige Beschichtungen als auch Phasenänderungen stellen Möglichkeiten zur Verbesserung der Brucheigenschaften dar. Dabei ist das Perlmutt von Muscheln das führende Modell um Brucheigenschaften zu verbessen indem harte und weiche Lagen abgewechselt werden.

In dieser Arbeit werden die mechanischen Eigenschaften von drei unterschiedlichen, selbst-organisierten, nanostrukturierten $Ti_{1-x}Al_xN$ Beschichtungen untersucht. Die, durch chemische Gasphasenabscheidung synthetisierten, Beschichtungen besitzen eine äußerst einzigartige Mikrostruktur, welche sich als Resultat des selbstorganisierten Wachstums bildete. Die Mikrostruktur wird durch Transmissionselektronenmikroskopie charakterisiert und die Phasenzusammensetzung wird mittels Röntgendiffraktion evaluiert. Die Morphologie der ersten Beschichtung zeigt eine Abwechslung von kubischer Struktur in den Ti-reichen und Wurtzit in den Al-reichen Nitrid-Phasen, wohingegen die zweite Beschichtung komplett aus kubischen Phasen aufgebaut ist. In der dritten Probe wurden die Phasen abgewechselt, was zu einer Multilagen-Beschichtung führt in der sowohl kubische und Wurtzit Al-reiche Phasen vorhanden sind.

Des Weiteren werden Härte und Indentationsmodulus mittels Nanoindentation charakterisiert. Für alle Proben werden E-Modul, Bruchspannung und Bruchzähigkeit mittels Biegebalkenexperimenten im Rasterelektronenmikroskop bestimmt. Diese Versuche wurden sowohl in in-plane Biegekraftorientierung, als auch in out-of-plane Biegekraftorientierung durchgeführt.

Die Ergebnisse zeigen herausragende mechanische Eigenschaften für alle drei Beschichtungen. Die Härte bewegt sich zwischen 26-37 GPa. Die Bruchspannung ist von den Phasen der nanostrukturierten Schichten abhängig und erreicht ein Maximum von 7.9 GPa in der Multilagen-Probe. Die Untersuchung des E-Moduls zeigt nahezu isotropes Verhalten für die monolithischen Schichten, wohingegen eine leichte Anisotropie in der Multilagen-Probe gefunden wurde. Für die Bruchzähigkeit wurde eine komplexe Abhängigkeit von der Schichtmorphologie festgestellt.

Des Weiteren wurde, sowohl durch Untersuchen des Rissfortschritts in den Multilagen-Strukturen während der in-situ Experimente, als auch durch die ex-situ Analyse der Bruchflächen ein besseres Verständnis für das Bruchverhalten von nanostrukturierten Dünnschichten erreicht.

Content

1. Introduction

1.1 Monolithic and Multi-Layered Hard Coatings

Transition metal nitride coatings have attracted significant industrial and scientific attention, because of their outstanding functional properties, such as high hardness and Young's modulus, good thermal stability, oxidation resistance and the ability to withstand a broad spectrum of chemical loads. The nitride coatings are usually synthesized using physical and chemical vapour deposition processes (PVD and CVD) [1–4].

In the 1980s, significant interest has been devoted to the synthesis of relatively simple coatings like TiN, CrN, SiN and ZrN [5–8]. These monolithic PVD coatings exhibit relatively low fracture toughness, originating primarily from the intergranular crack growth along elongated columnar grains. The recorded fracture toughness values were in the range of 1.6 – 3.8 $MPam^{½}$ [9–11].

With ever increasing industrial demands for higher cutting speeds and operating temperatures, there have been enormous efforts to develop coating materials with increased thermal stability and mechanical properties such as toughness and hardness. For this reason ternary and quaternary alloys like TiAlN, CrAlN, TiCrN, ZrAlN, CrTiN, CrSiN and TiAlSiN [12–15] have been developed and extensively characterized. Additionally there was also a great effort to develop micro-structured coatings based on multi-layer architecture and nanocomposite microstructure, resulting in fracture toughness up to ~2.70 $MPam^{½}$ [15–19].

Special attention has been devoted to the development of coatings with a high content of aluminium. The reason has been that during service, a dense top Al_2O_3 layer is formed at high temperatures in air at the coating surface, which protects the coating interior from oxygen diffusion, thus providing excellent oxidation resistance [20].

Since AlN is usually prepared in its soft hexagonal modification, there was an effort to synthetize hard coatings containing cubic AlN polytypes [19][21]. In the case of multi-layered coatings which contain AlN, the outmost values for hardness, and also fracture toughness have been measured in coatings, where the AlN phase had been stabilized in the metastable cubic structure. One way to stabilize this structure is to reduce the crystallite domain size and apply high coherency strains [16][17][19][22]. With typical growth rates of below one µm per hour for PVD coatings, however, the production of multi-layered coatings containing cubic AlN is time-consuming and expensive [16][23], which is a significant drawback in the industrial application of these coatings.

1.2 CVD Coatings with High Al Content

The CVD synthesis of Al-rich $Ti_{1-x}Al_xN$ coatings has attracted much attention in last 10 years. The motivation was to produce (i) **oxidation resistant** coatings using (ii) **large scale efficient** CVD deposition facilities. It was possible to produce (i) cubic monophasic coatings with Al ratio up to x = 90% [2] and (ii) *self-organized nano-lamellar* $Ti_{1-x}Al_xN$ coatings consisting of alternating cubic TiN and hexagonal AlN lamellae. One of the main advantages of CVD process is that deposition rates of more than 5µm/h can be achieved.

The synthesis and properties of unique self-organized nanolamellar cubic TiN / wurtzite AlN coatings were reported in 2014 by Todt *et. al* [24]. The coatings with Al content of 95% showed a relatively high hardness of ~26 GPa at temperatures up to 1000°C and excellent oxidation resistance. These properties were attributed to the unique nanolamellar coating microstructure. The further effort

concentrated on the optimization of the nanolamellar morphology and synthesis of pure cubic coatings with high Al content.

In 2016, CVD $Ti_{1-x}Al_xN$ coatings consisting of alternating cubic face-centred (fcc) AlN and TiN phases were reported by Todt. *et al* [25]. Although the newly developed $Ti_{0.2}Al_{0.8}N$ coating show a slightly decreased oxidation resistance compared to cubic-hexagonal coatings from Ref. [24], the phase stability remained relatively same, while at the same time a hardness increase up to 38 GPa was observed. Transmission electron microscopy (TEM) studies revealed a very unique microstructure based on columnar grains consisting of coherent nano-lamellae of AlN and TiN phases forming an irregularly faceted layered coating morphology. Obviously, cubic TiN stabilized AlN phase, thus resulting in the formation purely cubic coating with high Al volume fraction.

The most interesting feature in both types of self-organized coating [24], [25] is, however, that they consist of periodic arrangements of alternating nanolamellae, independent of the Al-content. Up to Al content of x = 0.8, the nanolamellae show a layer periodicity of 14 nm, with 12 nm fcc-AlN and 2 nm fcc-TiN. At Al contents above x = 0.8, AlN-phase occurs in stable wurtzite configuration. The layer periodicity is slightly smaller than in the cubic coatings with the total lamella thickness of 13 nm and AlN and TiN thickness of ~11 and ~2 nm.

The hardness values of ~26 and ~36 GPa obtained for $Ti_{0.05}$ $Al_{0.95}N$ and $Ti_{0.2}Al_{0.8}N$ document that the nanoscale variation of nanostructure and phases can be used to effectively tune mechanical properties of the self-organized coatings. Until now, however, there is no data available on the fracture response of those coatings.

1.3 Bioinspired Materials Concepts

Biological materials differ in many ways from most synthetic materials, primarily in (i) bottom-up-formation, (ii) self-organization, (iii) multifunctionality and (iv) hierarchy [26][27].

In exoskeletons, like those of molluscs, mother-of-pearl is an excellent example illustrating these properties: (i) the aragonite platelets grow from dissolved mineral, (ii) the growth is self-organized, restricting platelet size and protein content, (iii) it grows at the inner part of the shell acting as a chemical barrier and crack trap. In addition (iv) it possesses multiscale hierarchy beginning with the ordered crystallites in one platelet (at the nm scale), over the platelet size (the µm scale) up to the thickness of the mesolayers (at the mm scale) [27–30].

Biological materials can be divided into two classes: (i) soft structures, like collagen, wood, keratin, elastin, etc. and (ii) hard structures, consisting of hierarchically assembled minerals like aragonite, hydroxyapatite, calcite or even amorphous silica. In materials like bone, nacre and tooth, excellent fracture behaviour is achieved by a combination of these hard phases, which are separated by a small amount of soft proteins.

In the case of nacre (Figure 1), one of the strongest known biological materials, the remarkable hardness and toughness are achieved by combining hard and brittle aragonite crystallites with a small amount of ~5% of protein [28]. Mechanical tests showed that the soft regions are responsible for crack blunting and deflection which results in excellent fracture toughness up to 7±3 MPa $m^{½}$ [31].

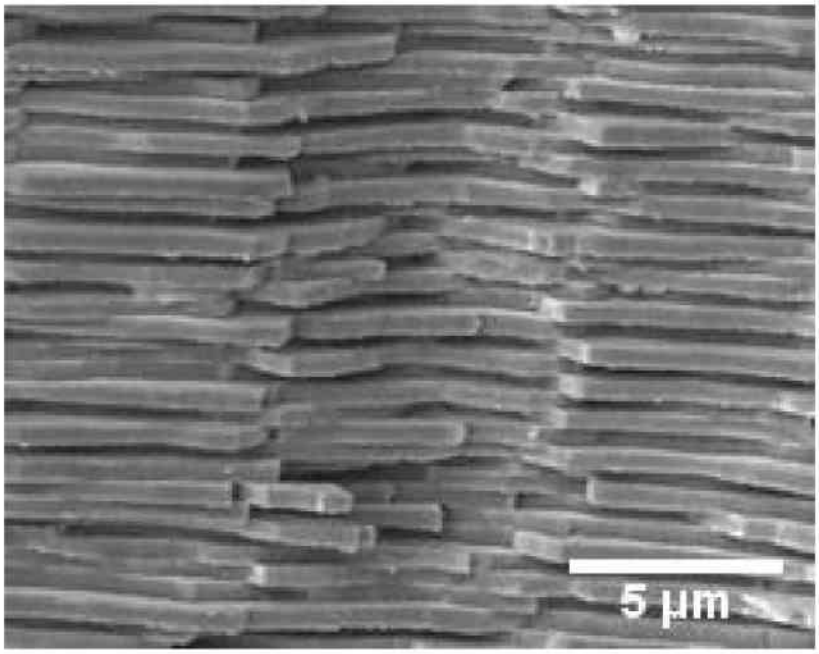

Figure 1. Scanning electron micrograph of brick and mortar structure of mother-of-pearl adopted from Barthelet and Espinosa [28]

Inspired by the combination of soft and hard materials in nacre, the already mentioned different mechanical properties of $Ti_{0.05}Al_{0.95}N$ [24] and $Ti_{0.2}Al_{0.8}N$ [25] coatings represent a good basis for further mechanical optimization of $Ti_{1-x}Al_xN$ coatings. The coatings themselves are (i) formed as a result of bottom-up-growth, as they are synthesized via CVD-growth, (ii) self-organized structures, because the AlN and TiN phases form an irregularly faceted layered coating morphology, (iii) multifunctional in terms of a diffusional barrier and mechanical protection and (iv) hierarchical, because of the different length scales in the organized microstructural features. Since $Ti_{0.05}Al_{0.95}N$ and $Ti_{0.2}Al_{0.8}N$ coatings possess different hardness, the coating materials were combined within one coating in order to develop a bioinspired, self-organized, nanolamellar and hierarchical soft-hard coating.

1.4 Micromechanical and Microstructural Characterization

In order to optimize the properties of protective coatings, it is necessary to apply advanced characterization techniques in order to determine how individual microstructural features influence the mechanical properties of coatings e.g. hardness and toughness. Those techniques have to operate at µm- or even sub-µm scale in order to assess the fracture behaviour of the coatings or their individual microstructural features.

For the microstructural characterization, state of the art techniques are: (i) transmission electron microscopy (TEM), (ii) scanning electron microscopy (SEM) and (iii) X-ray diffraction (XRD), which allow to determine volume-averaged as well as very local microstructural properties of materials, as demonstrated e. g. in [32–35].

In order to develop techniques for the quantitative characterization of mechanical properties of coatings like (i) fracture toughness, (ii) fracture stress and (iii) elastic modulus, a significant progress has been achieved within last 10 years. Experiments on features with sizes in µm and nm ranges are nowadays state of the art. With modern focused-ion-beam (FIB) based sample preparation it is possible to produce miniaturized samples for tensile, compression and bending tests, as demonstrated e. g. in [35–38].

In case of metals, tensile and compression tests are frequently used to assess the mechanical response of the material [33][39]. In the case of hard coatings, nanoindentation was established as standard technique providing local information on hardness and indentation modulus. Indentation experiments have also often been used to evaluate fracture properties of hard coatings [40][41]. One major drawback of these experiments is however, that the quantitative evaluation of fracture toughness values is prone to errors.

There has been significant effort (i) to characterize fracture properties very locally and (ii) to increase the reliability of the quantitatively evaluated elastic and fracture properties. Here, especially an in-situ cantilever bending method, which was already applied to other coating systems [9][10][11][36], represents an important tool.

1.5 Thesis Objectives

The aim of this work is to quantify superior mechanical properties of three self-organized, nanostructured, lamellar $Ti_{1-x}Al_xN$ coatings using advanced micromechanical testing approaches. Additionally, the quantitative mechanical characteristics are correlated with the unique coating microstructure in order to understand the differences in the mechanical response of these three nanostructures. For this purpose, the microstructures are characterized using advanced characterization techniques. Mechanical properties of the coatings are evaluated by in-situ cantilever bending tests to quantify in particular fracture toughness and fracture stress.

The main scientific objective is to quantitatively determine how the biomimetic design of the nacre-like $Ti_{1-x}Al_xN$ coating influences the material fracture properties.

2. Experimental Processes

In the following section, the experimental techniques and approaches (i) used for the sample preparation, (ii) sample characterization and (iii) experimental data collection are outlined. First the coatings were prepared by CVD by Boehlerit (Kapfenberg, Austria) using an industrial deposition plant. This was followed by transmission electron microscope imaging and X-ray diffraction characterization. In the next step, nanoindentation experiments were carried out on the samples. Finally micro-cantilevers were fabricated from the coatings and later fractured using in-situ micromechanical tests in the SEM.

2.1. Chemical Vapour Deposition (CVD) Preparation

In this work three coating systems were analysed. All three coatings consist of $Ti_{1-x}Al_xN$ and were deposited on WC-Co (6wt. %) cutting tool inserts serving as substrate.

2.1.1 $Ti_{0.05}Al_{0.95}N$ Coating

The $Ti_{0.05}Al_{0.95}N$ coating was deposited using CVD in a Bernex medium temperature MT-CVD-300 reactor. First bond layers of TiN and $Ti_{0.5}C_{0.5}N$ with thicknesses of 1 µm and 3.5 µm, respectively, were deposited on a WC-Co (6 wt. %) cutting tool insert as substrate. The deposition was performed at a temperature of 800°C using a pressure of 2.5 kPa, which represents low pressure chemical vapour deposition (LPCVD). The reactant gases were $AlCl_3$, $TiCl_4$, CH_3CN, N_2 and NH_3. H_2 was used as a carrier gas. The ratio of the applied precursors $AlCl_3$: $TiCl_4$ in the deposition chamber was 2.25. The $Ti_{0.05}Al_{0.95}N$ consisted of cubic Ti(Al)N and wurtzite Al(Ti)N nanolamellae. Figure 2 shows a cross-section of the $Ti_{0.05}Al_{0.95}N$ coating.

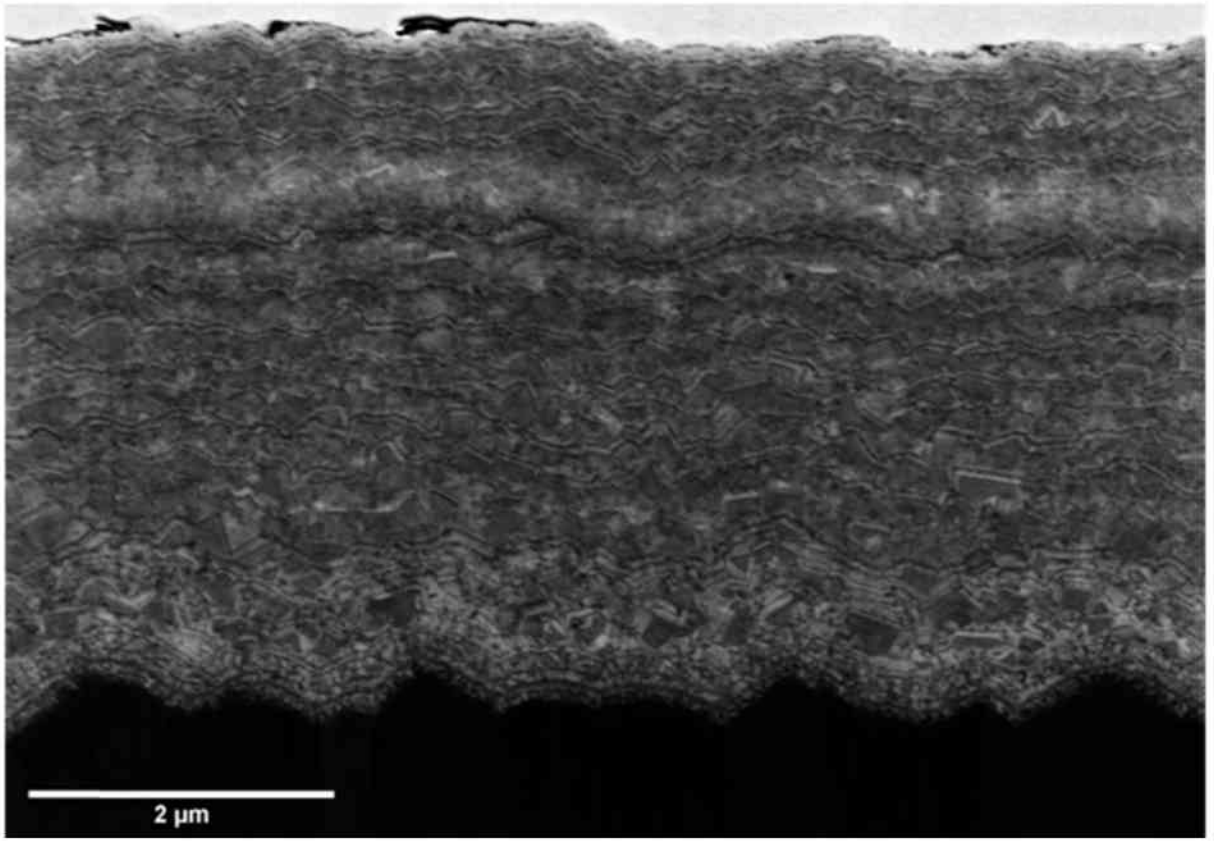

Figure 2. SEM image of a cross-section from $Ti_{0.05}Al_{0.95}N$ coating

2.1.2 $Ti_{0.2}Al_{0.8}N$ Coating

The $Ti_{0.2}Al_{0.8}N$ coating was deposited in a Bernex medium temperature MT-CVD-300 reactor on a WC-Co (6 wt. %) cutting tool insert as a substrate. First a TiN-bonding layer with a thickness of around 100 nm was grown. The deposition was done at a temperature of 800°C with a pressure of 2.5 kPa, using LPCVD. The reactant gases were $AlCl_3$, $TiCl_4$, N_2 and NH_3; H_2 was added as carrier gas. The ratio of the applied precursors $AlCl_3$: $TiCl_4$ in the deposition chamber was 0.9. The $Ti_{0.2}Al_{0.8}N$ coating consisted of cubic Ti(Al)N and cubic Al(Ti)N phases. Figure 3 shows a cross-section of the $Ti_{0.2}Al_{0.8}N$ coating.

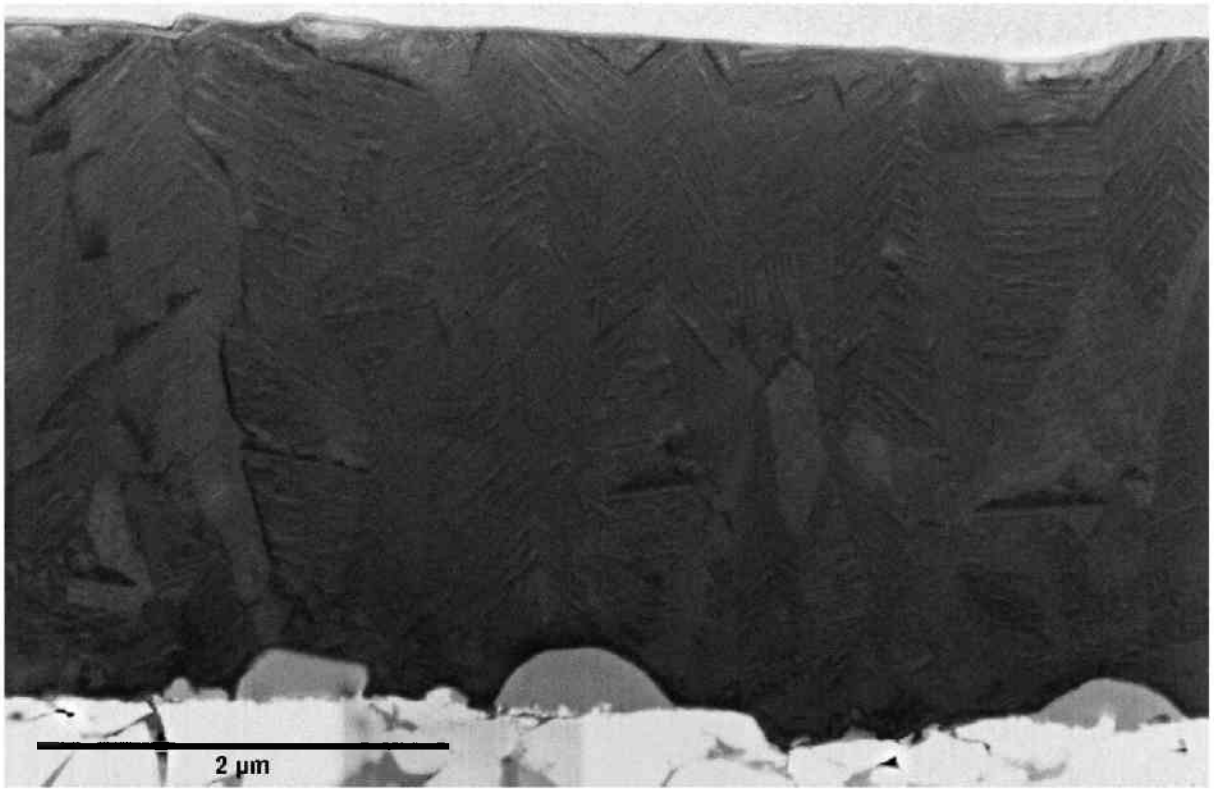

Figure 3. SEM image of cross-section from $Ti_{0.2}Al_{0.8}N$ coating

2.1.3 $Ti_{1-x}Al_xN$ Multi-Layered Coating

The third sample was prepared by alternating the former mentioned coating preparation processes leading to the formation of thicker $Ti_{0.2}Al_{0.8}N$ sublayers of ~500nm interrupted by thin layers of $Ti_{0.05}Al_{0.95}N$ of ~50 nm. The aim was to mimic the nacre microstructure by combining materials of different mechanical properties. Figure 4 shows a cross section of the $Ti_{1-x}Al_xN$ multi-layered coating.

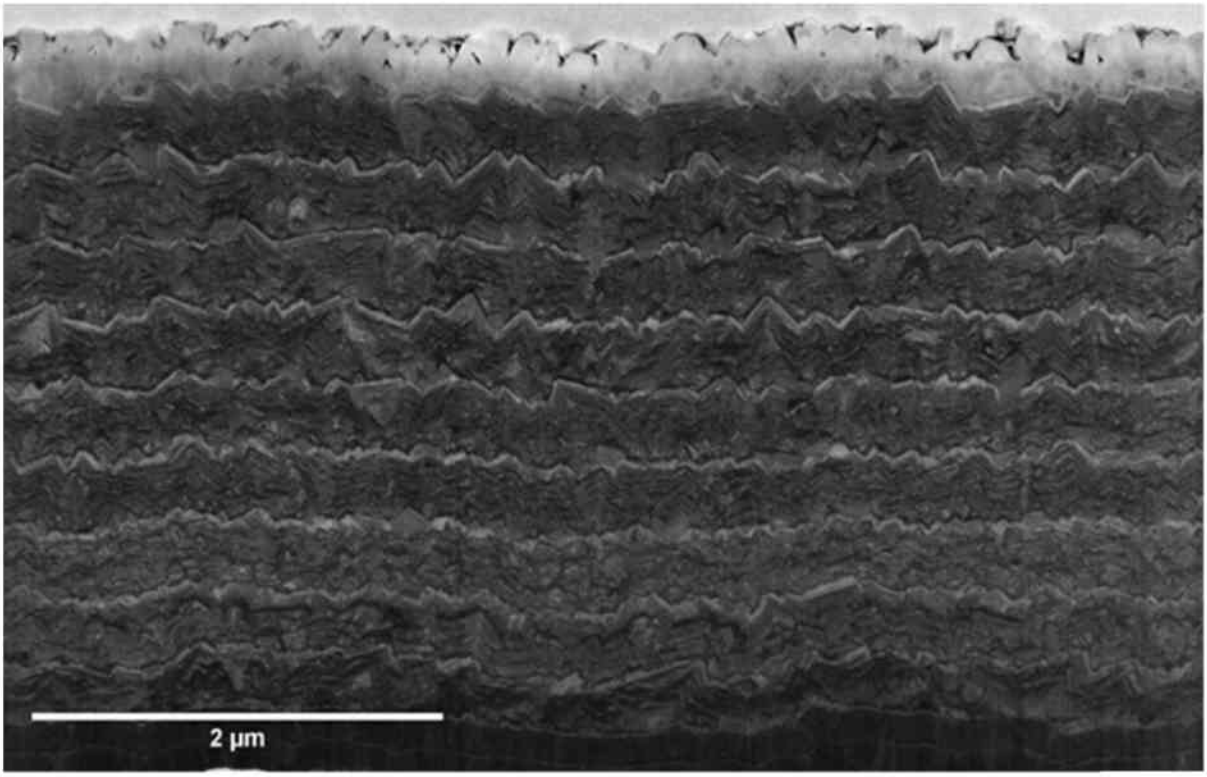

Figure 4. SEM image of a cross-section of $Ti_{1-x}Al_xN$ coating with nacre-like microstructure

2.2. X-ray Diffraction Characterization

XRD phase analysis of the samples was performed using a 5-circle X-ray diffractometer (SmartLab from Rigaku Co.) equipped with Cu-Kα radiation, a parabolic multilayer mirror in the primary beam and a secondary graphite monochromator. The XRD characterization was carried out in grazing incidence geometry using 1° incidence angle.

2.3. Microstructure Analysis using Transmission Electron Microscopy

The microstructure of the coatings was analysed using a high resolution transmission electron microscope (HR-TEM/STEM, JEOL 2100F) equipped with an imaging spherical aberration corrector (C_s) and a Tridiem imaging filter from Gatan that delivered point to point resolution better than 0.14 nm.

The cross-sectional TEM samples were prepared using focused ion beam (FIB) milling in a SEM-FIB dual beam unit Auriga workstation (Zeiss SMT). A low voltage of 2 kV at final stages of the preparation was used in order to minimize the sample amorphization.

2.4. Nanoindentation Characterization

Nanoindentation on the surface of the samples was carried out with a UMIS II (UltraMicro Indentation System) nanoindenter from Fischer-Cripps Laboratories, equipped with a Berkovich tip. The surface area was smoothened by a CALOTEST device using a very small force to overcome the surface roughness induced by the CVD deposition process. The indents were evaluated using the Oliver and Pharr method [42]. The evaluation method will be described in Chapter 3.6.

2.5 Micro-Cantilever Testing Geometry

All coatings were tested both in in-plane (Figure 5) as well as out-of-plane (Figure 6) orientation to evaluate a possible coating anisotropy by comparing the mechanical behaviour along the directions parallel and perpendicular to the substrate surface, respectively.

Figure 5 shows the orientation of the sample with respect to the applied force in **in-plane** configuration. In this case the applied force vector is oriented parallel to the coating surface. The evaluated elastic and fracture properties represent cross-sectional averages and are partly insensitive to the variation of cross-section (e.g. multi-layered) microstructure.

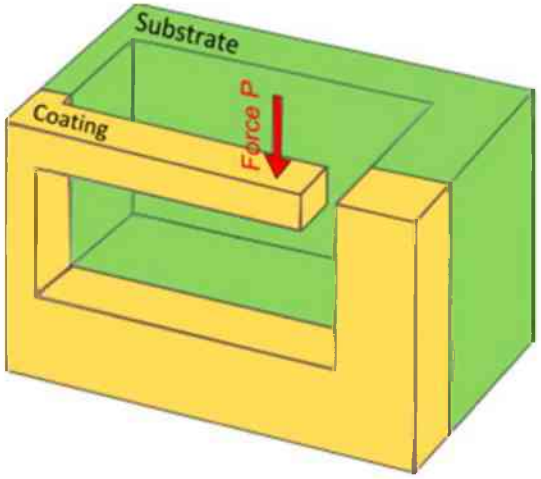

Figure 5. Force direction for in-plane cantilever testing orientation.

Figure 6 shows the orientation of the sample with respect to the applied force in **out-of-plane** configuration. In this configuration the force vector is oriented perpendicular to the coating surface and the evaluated elastic and fracture properties reveal the influence of a coating cross-sectional microstructure gradient.

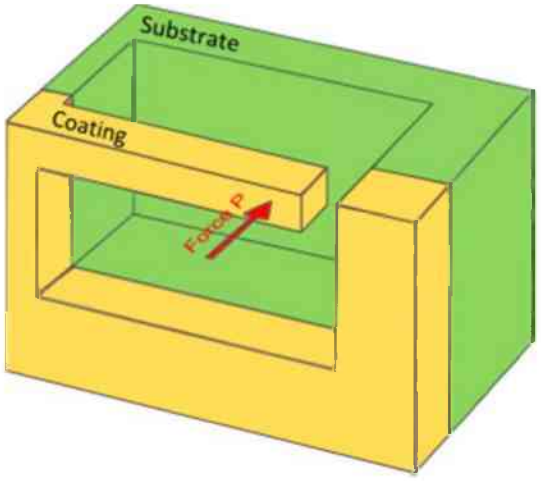

Figure 6. Force direction for out-of-plane cantilever testing orientation.

2.6. Micro-Cantilever Fabrication

The micro-cantilevers for micromechanical tests of the coatings were machined using a SEM-FIB dual beam unit Auriga workstation (Zeiss SMT) at the Material Center Leoben GmbH in Leoben.

The cantilevers were milled from the surrounding material in five steps. At first, a rough in-plane cut was performed to remove the substrate below the cantilever (Figure 7). Also a surface region of the coating was removed in this step, because of its roughness and the presence of redeposited material. To get a uniform sample and to eliminate effects of the substrate-coating interface, ~500 nm of the coating was removed from the coating-substrate interface. The same was done for the coating surface region.

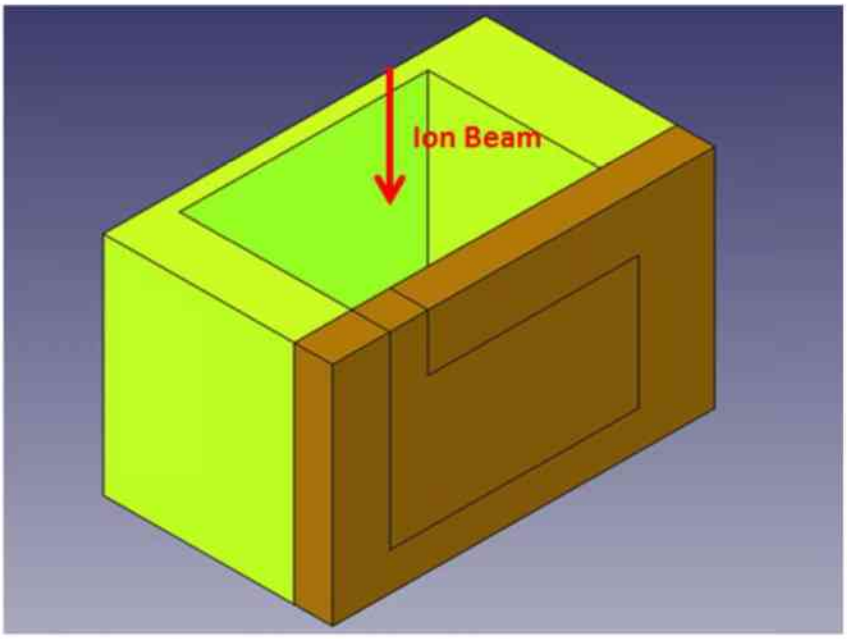

Figure 7. A schematic sketch of the first step to produce a cantilever for micromechanical test – the substrate remove.

As a second step, the cantilever was cut out in the out-of-plane ion beam orientation (Figure 8). Also, in this step the cantilever was set back from the surface to exclude the influence of the surface roughness. The first and the second step were performed with a beam current of 4 nA.

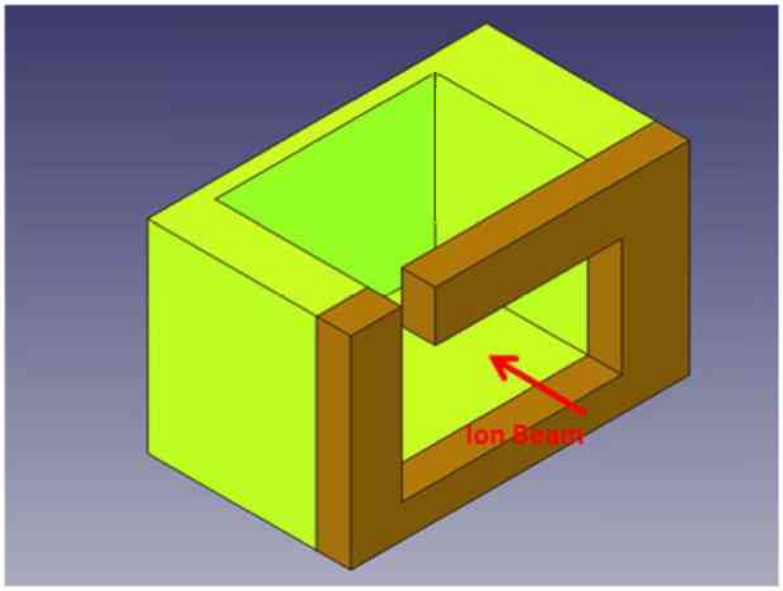

Figure 8. A schematic sketch of the cantilever machined using FIB.

In the next sequence of cuts, cantilevers were precisely shaped using an ion current of 600 pA. Again, one out-of-plane (c.f. Figure 8) and one in-plane (c.f. Figure 7) FIB-cut were carried out on the cantilever. The final desired cantilever geometry comprised a length of 10 µm and a cross section of 4 µm², with the width and the thickness both having 2 µm. Based on this geometry 10 cantilevers were produced for every coating type. In the final step, a notch was added to six of the cantilevers using a 5 pA current for around 5–10s of the machining time. For one half of the notched cantilevers, the notches were placed on the coating surface (for the out-of-plane testing) while, for the second half, the notches were placed on the cantilever cross-sections (for the in-plane testing). In Figure 9, an exemplary set of FIB-fabricated cantilevers is presented.

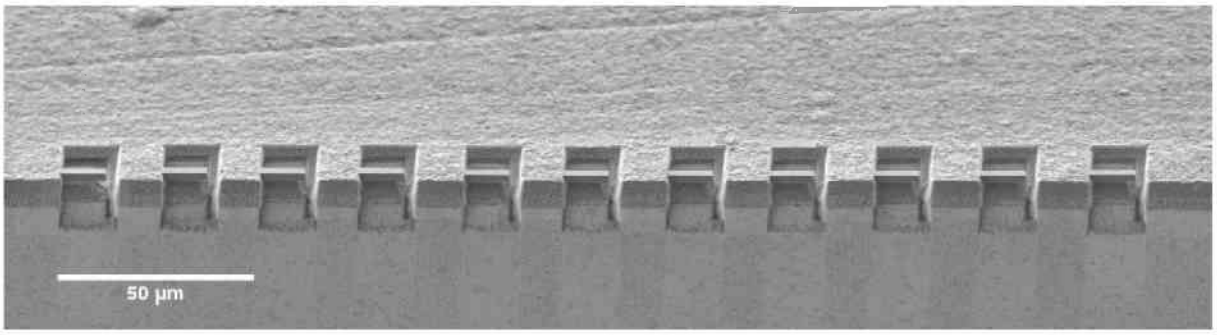

Figure 9. An exemplary array of FIB-machined cantilevers with dimensions of ~2x2x10 µm^3.

Figure 10 shows a $Ti_{0.05}Al_{0.95}N$ cantilever before testing. The visible cantilever surface shows a part of the coating cross-section presented in Figure 2.

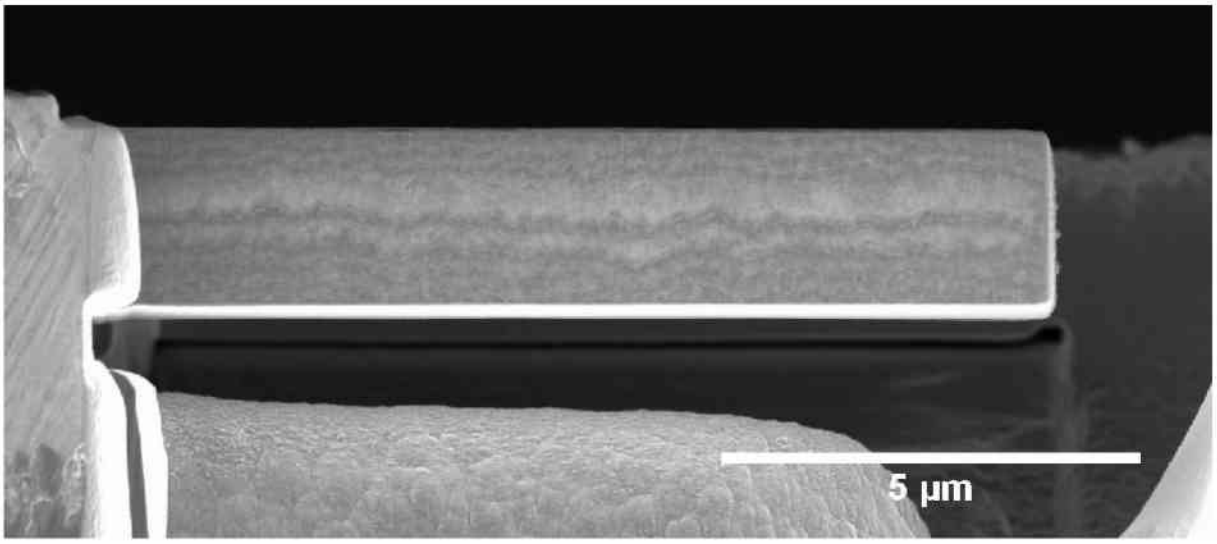

Figure 10. SEM image of cantilever cross-section machined from $Ti_{0.05}Al_{0.95}N$ coating.

Figure 11 shows a $Ti_{0.2}Al_{0.8}N$ cantilever prepared for testing. The visible cantilever surface shows a part of the coating cross-section presented in Figure 3.

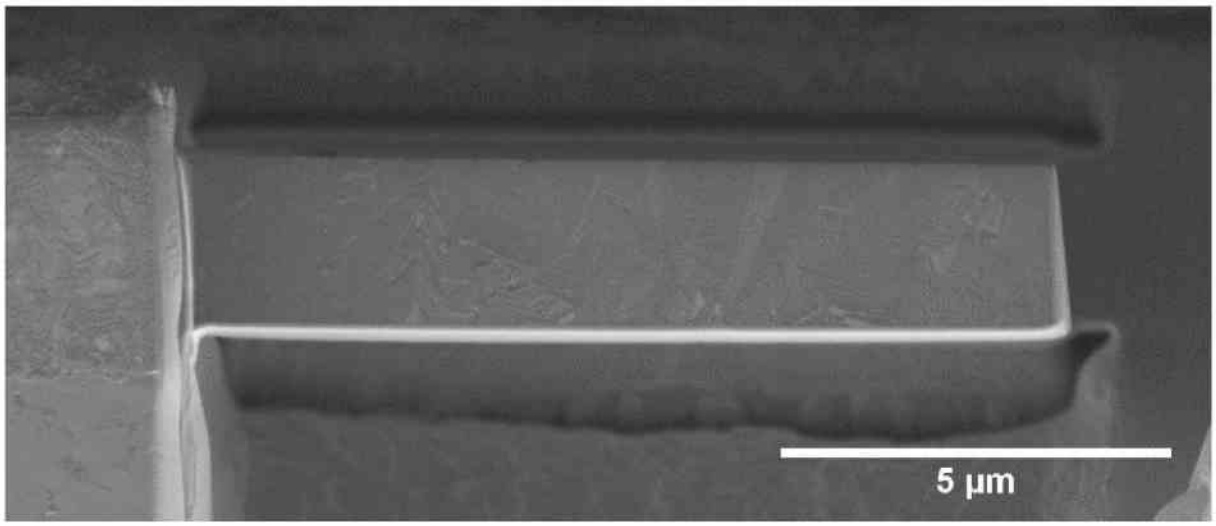

Figure 11. SEM image of cantilever cross-section machined from $Ti_{0.2}Al_{0.8}N$ coating.

Figure 12 presents a $Ti_{0.2}Al_{0.8}N$ cantilever prepared for testing. The visible cantilever surface shows a part of the coating cross-section presented in Figure 4.

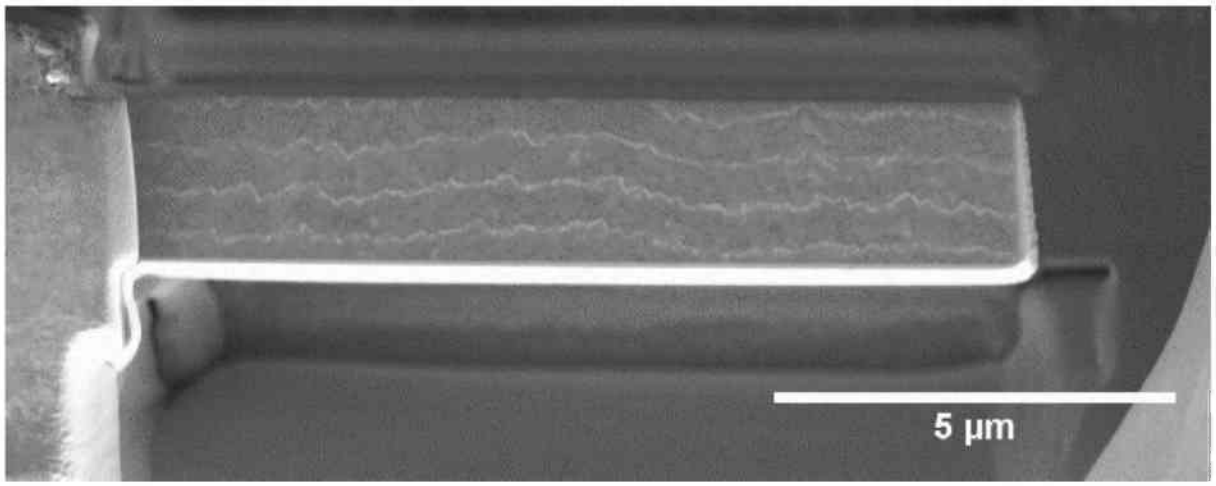

Figure 12. SEM image of cantilever cross-section machined from $Ti_{1-x}Al_xN$ coating with nacre-like microstructure.

2.7. In-Situ Testing

All in-situ experiments on micro-cantilevers were performed in a Zeiss Leo SEM 982 scanning electron microscope. In order to apply the bending moment, a Hysitron PI85 indenter system, equipped with a sphero-conical indenter tip with a radius of 0.7 µm was used.

Figure 13 shows the indenter system as it is mounted on the SEM stage with the transducer on the left, the indenter tip in the middle and the piezo stage with the sample mounted on it on the right side. The movement of the indenter system is independent from the SEM stage movement, implying, that if the indenter tip is positioned in the middle of the SEM image, it is possible to position the sample with the whole piezo stage of the Hysitron system. The indenter tip is able to move 5 µm in the forward direction, while the piezo stage can be moved to position the cantilever accurately.

After the sample is positioned, the load function (displacement over time) is predefined in the delivered software and, afterwards, the cantilever bending test can be performed automatically.

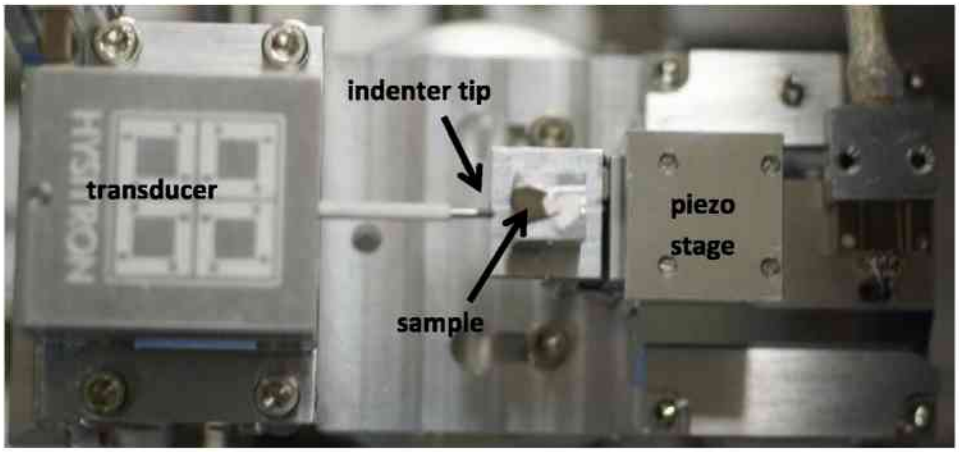

Figure 13. Hysitron PI85 indenter system with a sample attached is presented.

The experiments were performed in displacement-controlled mode with the loading speed $\dot{w}_t$ of 20 nm/s. All cantilevers were loaded until fracture occurred. The system recorded load-displacement curves for every bending experiment, and all experiments were also recorded with a video graphics unit.

The loading speed was chosen in such a way that the strain rate $\dot{\varepsilon}_x(L)$ at the constraint of the cantilever was held in a range of 10^{-3} s^{-1}.

The selected geometry of the cantilevers was (Figure 13)

$$L = 10\ \mu m \qquad t = 2\ \mu m \qquad B = 2\ \mu m.$$

The strain rate can thus be calculated to be (c.f. section 3.4)

$$\dot{\varepsilon}_x(L) = \frac{3t\dot{w}_t}{2L^2} = 6 \times 10^{-4}\ s^{-1} \sim 10^{-3}\ s^{-1}. \qquad (1)$$

In Figure 14, a sequence of SEM micrographs shows a $Ti_{1-x}Al_xN$ cantilever before and during the experiment as well as after fracture with the cantilever fractured at the notch.

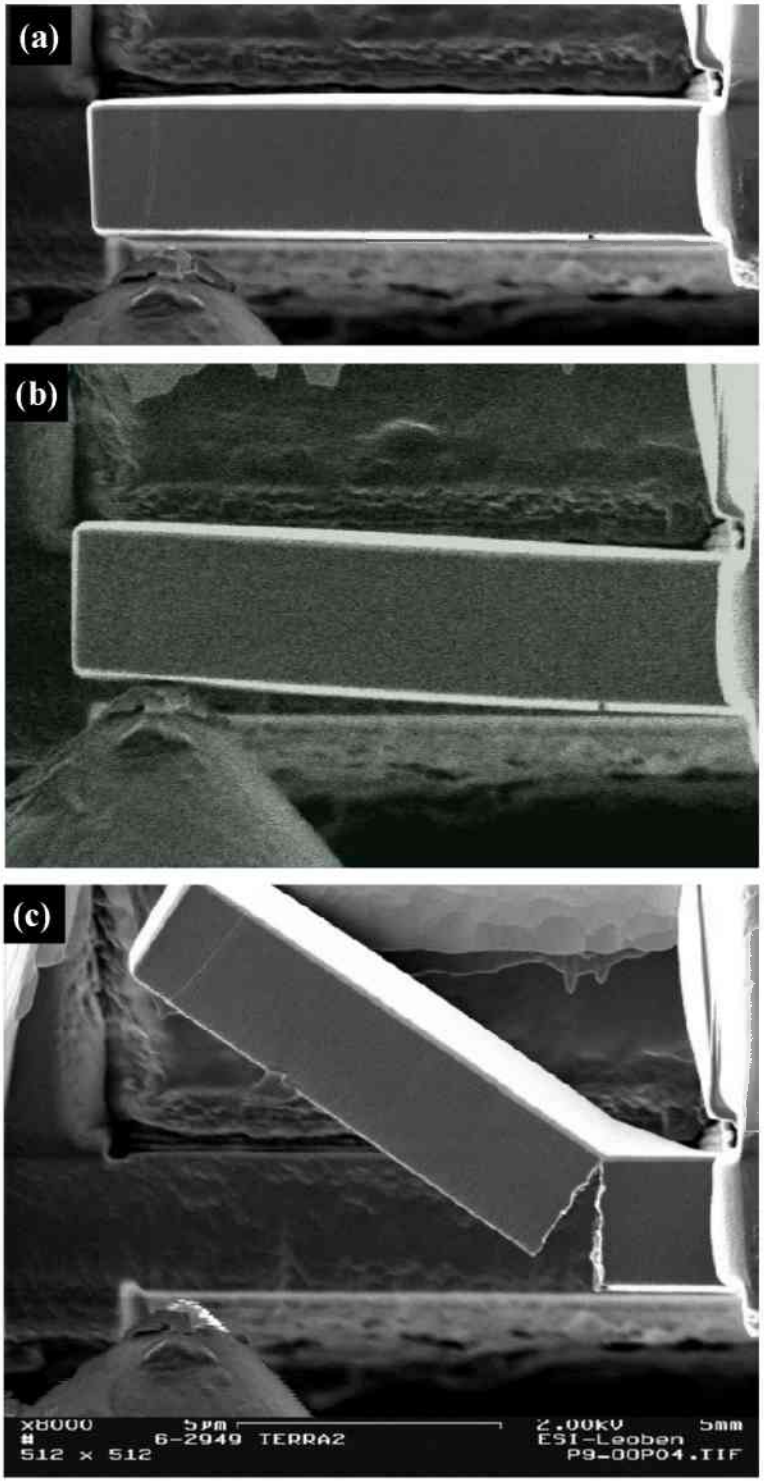

Figure 14. From top to bottom: Cantilever before (a) and during loading (b), the last picture shows the fractured cantilever (c).

2.8. SEM Analysis of Fracture Surfaces

The fracture surface of the cantilevers was evaluated ex-situ in the SEM Zeiss LEO 1525, applying a voltage of 2kV and the image was taken using an in-lens detector.

3. Evaluation Method

In the following section, first the evaluation of the elastic properties is presented based on the Euler-Bernoulli beam theory, which is described in Refs. [43][44]. This is a continuum mechanical theory which is well-known and suitable for describing these experiments [9][10][36][38]. Afterwards the evaluation of the fracture toughness experiments is shown, which is specified in Ref. [45] and finally the Oliver-Pharr method for evaluation of hardness is pointed out.

3.1 Schematic Representation and Calculations needed for the Experiment

Figure 15 shows a schematic sketch of a cantilever experiment outlining the overall geometry. *t* represents the thickness of the cantilever parallel to the loading direction, *B* is the width, normal to the loading direction. *L* is the bending length of the cantilever. $\vec{P}$ represents the force with which the cantilever is loaded.

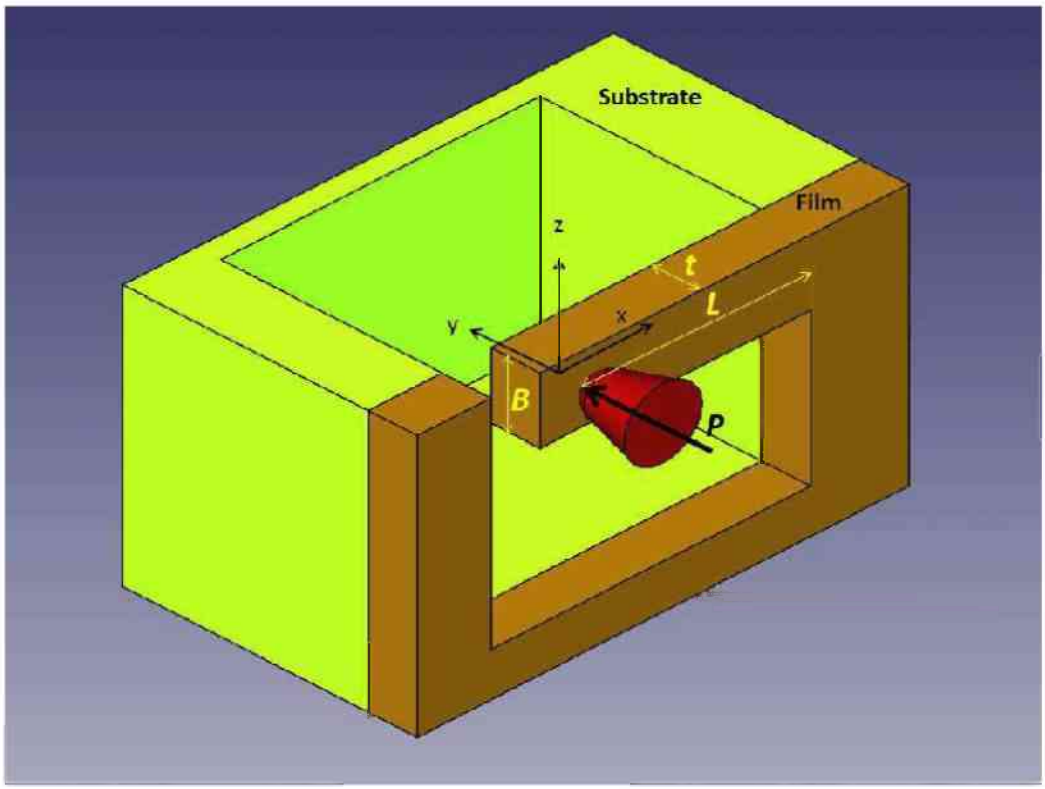

Figure 15. Schematic representation of the bending experiment with the definition of important dimensions and parameters

First the free-body diagram for the cantilever has to be constructed. The coordinate system has its origin in the centre of the cantilever and the force $\vec{P}$ is parallel to the *y*-axis. The force and the running coordinate $\vec{x}$ are defined as follows

$$\vec{P} = \begin{pmatrix} 0 \\ P \\ 0 \end{pmatrix} \tag{2}$$

$$\vec{x} = \begin{pmatrix} x \\ 0 \\ 0 \end{pmatrix}. \tag{3}$$

At any position *x*, which is represented by the running coordinate, the cantilever can be subjected to an imaginary cut. At each cutting point of the cantilever the inner reactional force $\vec{N}$ and torque $\vec{M}$

have to be applied, using the condition that the cantilever as a whole has to be in kinematic equilibrium.

The force equilibrium at the position $\vec{x}$ in the cantilever is

$$\vec{P} + \vec{N} = \vec{0}. \tag{4}$$

Therefore the inner reactional force $\vec{N}$ is

$$\vec{N} = -\vec{P} = -\begin{pmatrix} 0 \\ P \\ 0 \end{pmatrix}. \tag{5}$$

The components of $\vec{N}$ are defined as follows

$$N_x = 0, \qquad N_y = -P, \qquad N_z = 0. \tag{6}$$

The torque equilibrium at the position $\vec{x}$ in the cantilever is

$$\vec{x} \times \vec{P} + \vec{M} = \vec{0}. \tag{7}$$

Therefore the inner reactional bending torque for a cantilever which is loaded at the position $\vec{0}$, can be stated as the origin of the coordinate system, with a load of $\vec{P}$ in direction of *y* and at the position *x*

$$\vec{M} = -\vec{x} \times \vec{P} = -\begin{pmatrix} x \\ 0 \\ 0 \end{pmatrix} \times \begin{pmatrix} 0 \\ P \\ 0 \end{pmatrix} = \begin{pmatrix} 0 \\ 0 \\ -Px \end{pmatrix}. \tag{8}$$

This leads to the components of $\vec{M}$, which are

$$M_x = 0 \qquad M_y = 0 \qquad M_z = -Px. \tag{9}$$

The second moment of area around the *z*-axis is the geometrical resistance against bending. It is stated in Ref.[43] [chapter 2.4, equation 2.116] and given by the equation (10), which can be solved as

$$I_z = \int y^2 dA = \iint y^2 dy dz = \iint_{-\frac{t}{2}}^{\frac{t}{2}} y^2 dy dz = \int_{-\frac{B}{2}}^{\frac{B}{2}} \frac{t^3}{12} dz = \frac{Bt^3}{12}. \tag{10}$$

In addition, the complementary energy U^* is a measure for the energy induced in an object by deformation. It is defined by the following equation, stated in Ref.[43] [chapter 5, equation 5.48], as

$$U^* = \frac{1}{2} \int_0^L \left(\frac{N^2}{EA} + \frac{M_y^2}{EI_y} + \frac{M_z^2}{EI_z} \right) dx. \tag{11}$$

As it was derived above, the bending torque around the *y*-axis is zero. For the evaluation of the stress and the Young's Modulus the proof has to be made, that one can treat the cantilever as a long beam. This proof can be done by comparing the complementary energy $U^*(N)$ (due to the lateral force N) to the complementary energy $U^*(M_z)$ (due to the bending torque M_z) as they are stated in Eq. 11 above. It can be assumed that

$$U^*(N) \ll U^*(M_z), \tag{12}$$

$$\int_0^L \frac{N^2}{A} dx \ll \int_0^L \frac{M_z^2}{I_z} dx. \tag{13}$$

Integrating both sides in Eq. 13 leads to

$$\frac{P^2}{Bt} L \ll 4 \frac{P^2 \times L^3}{B \times t^3}. \tag{14}$$

Rearranging Eq. 14 leads either to Eq. 15 or Eq. 16

$$t \ll 2L, \tag{15}$$

$$\frac{t}{L} \ll 2. \tag{16}$$

In the present case the ratio of t to L is of course about 0.2. The same goes for the B-to-L ratio. Substituting this into Eq. 14 and calculating the two energies results in

$$\frac{P^2}{0.2 \times 0.2 \times L^2} \ll 4 \frac{P^2 \times L^2}{0.2^4 L^4}. \tag{17}$$

Calculating the factors for both sides leads to

$$25 \frac{P^2}{L^2} \ll 2500 \frac{P^2}{L^2}. \tag{18}$$

This means, that the energy due to the bending torque is around 100 times larger than the energy due to the lateral force, which in turn implies that the cantilevers can be treated as long beam (with respect to the thickness) and that the part of the lateral force is negligible.

Furthermore, the bending line of the cantilever has to be calculated. The second derivative of the bending line is proportional to the bending torque as is stated in Ref.[43]. The proportionality factor is given as Young's modulus E times the second moment of area I_z:

$$-EI_z \frac{\partial^2 w(x)}{\partial x^2} = M_z(x). \tag{19}$$

Using the definition of M_z from Eq. 9 in Eq. 19 leads to

$$-EI_z \frac{\partial^2 w(x)}{\partial x^2} = -Px, \tag{20}$$

which can be written as

$$\frac{EI_z}{P} \frac{\partial^2 w(x)}{\partial x^2} = x. \tag{21}$$

Both sides are then integrated over two times, resulting in:

$$\frac{EI_z}{P}\frac{\partial w(x)}{\partial x} = \frac{x^2}{2} + C_1, \tag{22}$$

$$\frac{EI_z}{P}w(x) = \frac{x^3}{6} + C_1 x + C_2. \tag{23}$$

The kinematic boundary conditions for the fixed cantilever are stated on p. 198 in Ref. [43]. These state, that at the position L on the cantilever, the deflection $w(L)$ as well as the first derivation of deflection $\frac{\partial w(L)}{\partial x}$ are zero.

$$\frac{\partial w(L)}{\partial x} = 0 \tag{24}$$

$$w(L) = 0 \tag{25}$$

Using both Eq. 24 and Eq. 25 in Eq. 23 the constants C_1 and C_2 can be evaluated as

$$C_1 = -\frac{L^2}{2}, \tag{26}$$

$$C_2 = \frac{L^3}{3}. \tag{27}$$

Finally this results in the expression for the deflection $w(x)$ of the cantilever:

$$w(x) = \frac{PL^3}{6EI_z}\left(\left(\frac{x}{L}\right)^3 - 3\left(\frac{x}{L}\right) + 2\right) \tag{28}$$

3.2 Young's Modulus

The derivation of the Young's modulus will be done with the complementary energy U^* (Eq. 11) and using Castigliano's method (Eq. 29), which states that the derivative of the complementary energy with respect to the force is the deflection regarding to this force [cf. Eq. 5.43 and Eq. 5.48 in Ref. [43]].

As it has been stated above for the cantilever beam, one can neglect the Force N and the bending torque M_y around the y axis is zero. The force F_i can be set as loading force P, and P clearly doesn't depend on the co-ordinate x.

$$U^* = \frac{1}{2}\int_0^L \left(\frac{M_z^2}{EI_z}\right) dx \tag{11}$$

$$\frac{\partial U^*}{\partial F_i} = w_i \tag{29}$$

Eqs. 9, 10 and 11 can be substituted in Eq. 28 which leads to Eq. 29:

$$w_i = \frac{\partial U^*}{\partial F_i} = \frac{1}{2}\int_0^L \frac{\partial}{\partial P}\left(\frac{12(-Px)^2}{EBt^3}\right) dx \tag{29}$$

The variables E, B and t depend neither on x or P, so they can be expressed as factors in Eq. 20. Also x doesn't depend on P and vice versa. This leads to the following equation

$$w_i = \frac{6}{EBt^3}\frac{\partial(P^2)}{\partial P}\int_0^L x^2 dx. \tag{30}$$

Solving Eq. 30 leads to the result for the deflection w_i of a cantilever under a force P in terms of parameters E, B, L, t:

$$w_i = \frac{4PL^3}{EBt^3}. \tag{31}$$

Referring to two arbitrary points in the elastic regime during the bending test, one can define Eq. 32 as follows

$$\Delta w = w_2 - w_1. \tag{32}$$

Accordingly, the difference in forces at these points is defined to be

$$\Delta P = P_2 - P_1. \tag{33}$$

Substituting Eqs. 31 and 33 into Eq. 32 results in

$$E = \frac{4}{B}\frac{\Delta P}{\Delta w}\left(\frac{L}{t}\right)^3. \tag{34}$$

Equation 33 gives an expression for the bending Young's Modulus, which relies only on cantilever beam geometry and the deflection of the load-displacement curve in the experiment.

3.3 Bending Stress

Bending stress is defined as following [cf. Eq. 4.31 in Ref.[43]]

$$\sigma_x(x,y) = \frac{M_z}{I_z} y. \tag{35}$$

The cantilever geometry restricts *y* to

$$-\frac{t}{2} < y < \frac{t}{2}. \tag{36}$$

Therefore the maximum tensile stress occurs at the outer fibre which has the *y* co-ordinate of

$$y = -\frac{t}{2}. \tag{37}$$

Substituting Eqs. 9 and 37 in Eq. 35 results in the maximum tensile stress σ_{max}

$$\sigma_{max}(x) = 6\frac{Px}{Bt^2}. \tag{38}$$

The cantilever geometry is restricted in *x*-direction,

$$0 < x < L, \tag{39}$$

it follows that utmost maximum tensile stress of the outer fibre occurs at

$$x = L. \tag{40}$$

The maximum tensile stress, the fracture stress σ_F is thus applied at the restraint of the cantilever as is shown in Eq. 41,

$$\sigma_F = 6\frac{P_{max}L}{Bt^2}, \tag{41}$$

where P_{max} is the maximum force applied on the cantilever at the moment of fracture.

3.4 Bending Strain

The bending strain according to the theory of Euler and Bernoulli is defined as followed [cf. pp. 10-15, Ref. [44]]:

$$\varepsilon_x(x,y) = -y\frac{\partial^2 w(x)}{\partial x^2} \tag{42}$$

Substituting Eq. 20 from chapter 3.1 and Eq. 31 from chapter 3.2 into Eq. 42 provides

$$\varepsilon_x(x,y) = -y\frac{\partial^2 w(x)}{\partial x^2} = -\frac{12yxP}{EBt^3} = -\frac{3w_i yx}{L^3} \tag{43}$$

As has been shown in Eq. 35, the *y* co-ordinate of the cantilever is constrained to

$$-\frac{t}{2} < y < \frac{t}{2}. \tag{36}$$

Also the *x*-coordinate has to be within the boundaries of

$$0 < x < L. \tag{40}$$

These boundary conditions are the same as in chapter 3.3, the maximum bending strain can be calculated as

$$\varepsilon_x(x) = \frac{3tw_i}{2L^3}. \tag{44}$$

The factor w_i (Eq. 31) in Eq. 44 represents the deflection of the cantilever at the position of the loading, which is measured during the experiment. The maximum strain therefore occurs at the restraint of the cantilever. The same is true for the maximum stress. Therefore it is possible to draw a representative stress-strain diagram for bended cantilevers, in the same fashion one does for tensile experiments [cf. examples in Refs. [28][30]].

3.5 Fracture Toughness K_{Ic}

For fracture toughness experiments a notch has to be added to the cantilever. Figure 16 shows a schematic representation of the cantilever experiment; the length *L* is now the distance between the loading point and the notch. The depth of the notch is described by parameter *a*.

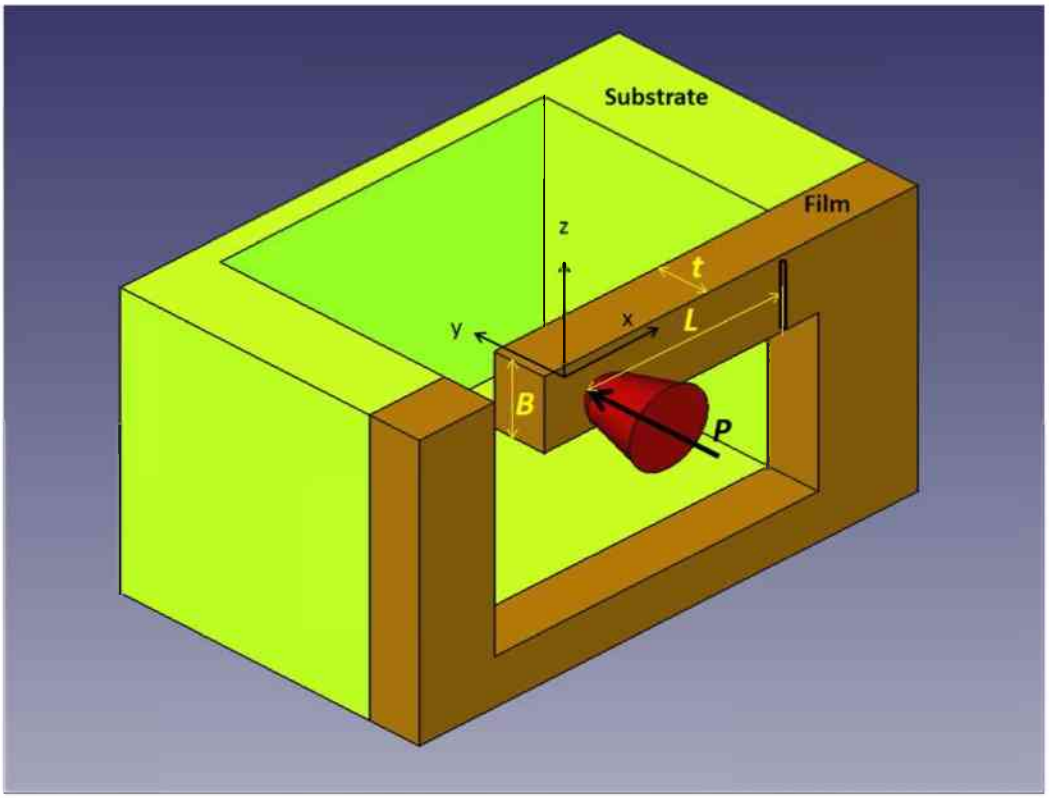

Figure 16. Schematic representation of the fracture toughness experiment with the definition of important dimensions and parameters

Linear elastic facture mechanics was used for evaluating the experiment [45]. The stress-intensity factor for Mode I, K_I, is defined as

$$K_I = \sigma\sqrt{\pi a} \times Y\left(\frac{a}{t}\right) \tag{45}$$

In Eq. 45, σ is the stress applied to the cantilever, a is the notch depth and Y is a dimensionless geometry factor, which is necessary, when the notch cannot be assumed to be small with regards to the cantilever dimensions. The fracture toughness K_{Ic} is now the stress intensity factor at the moment of fracture and as such a material parameter.

$$K_{Ic} = K_I(\text{fracture}) \tag{46}$$

The dimensionless geometry factor Y is defined in [46] for the given beam shape. It depends only on the notch depth a and the thickness t of the cantilever:

$$Y\left(\frac{a}{w}\right) = \sqrt{\frac{2t}{\pi a}\tan\frac{\pi a}{2t}}\,\frac{0.923+0.199\left(1-\sin\left(\frac{\pi a}{2t}\right)\right)^4}{\cos\left(\frac{\pi a}{2t}\right)}. \tag{47}$$

Substituting Eqs. 45, Eq. 47 and Eq. 41 leads to

$$K_{Ic} = 6\frac{P_{max}L}{Bt^2}\sqrt{\pi a}\sqrt{\frac{2t}{\pi a}\tan\frac{\pi a}{2t}}\frac{0.923+0.199(1-\sin(\frac{\pi a}{2t}))^4}{\cos(\frac{\pi a}{2t})}, \tag{48}$$

which is an expression for the fracture toughness K_{Ic}, which can be calculated from measurable parameters of the experiment.

After the evaluation of the fracture toughness a validity condition has to be applied, which is defined as

$$a, B, t > 2.5\left(\frac{K_{Ic}}{\sigma_{ys}}\right)^2. \tag{49}$$

This equation is stated in Ref. [45] [cf. Eq. 4.67 on page 90]. In Eq. 49 the variable σ_{ys} is the yield strength of the material. In the experiments the yield strength was substituted by the fracture stress of the material, because the yield stress had not been evaluated. Also small-scale yielding has to be considered, which is described in Chapter 4.7, also in [45]. According to this theory the effective crack length a_{eff} is larger than the notch depth a by the amount of the radius of the plastic zone r_p. This is named Irwin's crack length correction:

$$a_{eff} = a + r_p. \tag{50}$$

The radius of the plastic zone is defined as

$$r_p = \frac{1}{2\pi}\left(\frac{K_I}{\sigma_F}\right)^2 \tag{51}$$

The effective crack length is then used instead of the former crack length, given by the notch depth a for evaluating the fracture toughness. The theory of small-scale yielding can be applied given that following condition holds

$$r_p \lesssim 0.02\{a, t-a, B\}. \tag{52}$$

If the conditions of Eq. 48 and 51 are satisfied, the fracture toughness can be stated as

$$K_{Ic} = 6\frac{P_{max}L}{Bt^2}\sqrt{\pi a_{eff}}\sqrt{\frac{2t}{\pi a_{eff}}\tan(\frac{\pi a_{eff}}{2t})}\frac{0.923+0.199(1-\sin(\frac{\pi a_{eff}}{2t}))^4}{\cos(\frac{\pi a_{eff}}{2t})}. \tag{53}$$

3.6 Oliver-Pharr Method for Nanoindentation

The subsequent nanoindentaion experiments performed in this work were evaluated by the method of Oliver and Pharr [42][47]. In the following section this approach for evaluating the reduced modulus and indentation hardness is briefly outlined.

Figure 17 depicts a graph of an indentation experiment as it was originally designed by Oliver and Pharr, showing the loading and unloading curve. In the diagram the load P is plotted against indentation depth h. The graph also shows the maximum indentation depth h_{max}, the maximum force P_{max}, the stiffness S and the contact depth h_C

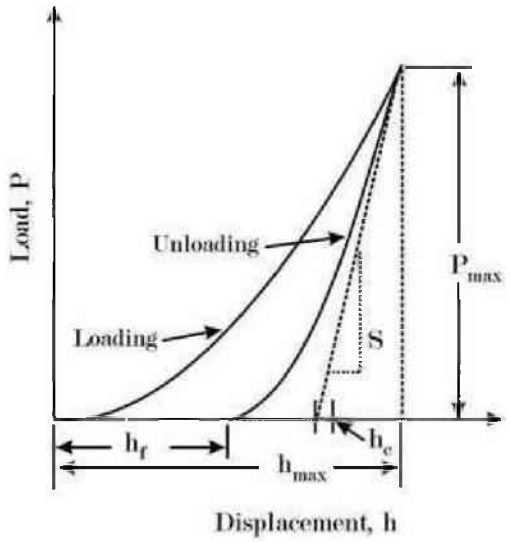

Figure 17. A schematic representation of load – displacement plot from a nanoindentation experiment with important dimensions and parameters is presented.

The hardness H is calculated using P_{max} and the contact area of the indent A, where A is a function of the contact depth h_C:

$$H = \frac{P_{max}}{A(h_c)}. \tag{54}$$

For evaluating the contact area the following relationship is used:

$$A(h_c) = 24.5\, h_c^2 + C_1 h_c^1 + C_2 h_c^{0.5} + C_3 h_c^{0.25} + \cdots + C_8 h_c^{1/128} \tag{55}$$

Here the leading term represents A for a perfect Berkovich indenter, while the other terms describe the deviations from that geometry.

In addition, the reduced modulus can be calculated as

$$E_r = \frac{1}{2}\sqrt{\frac{\pi}{A}}S, \tag{56}$$

where A is the contact area and S is the stiffness as shown above. The indentation modulus E can be calculated using

$$\frac{1}{E_r} = \frac{(1-\nu^2)}{E} + \frac{(1-\nu_i{}^2)}{E_i}, \tag{57}$$

where ν is the Poisson's number of the indented material, E_i and ν_i are the Young's modulus and Poisson's number of the indenter.

4. Experimental Results

In the following section the results of the former outlined experimental setups are presented. First the phases present in the coatings are analysed using XRD, then the microstructure is characterized using TEM, afterwards the hardness and indentation modulus results are presented. Finally the mechanical properties, such as Young's modulus, fracture stress and fracture toughness are listed.

4.1 XRD Phase Analysis

In this section the results from the XRD-phase analysis of the coatings are presented, beginning with the $Ti_{0.05}Al_{0.95}N$-coating, followed by the $Ti_{0.2}Al_{0.8}N$-coating and the combined multi-layered nacre-like $Ti_{1-x}Al_xN$ coating.

4.1.1 XRD on $Ti_{0.05}Al_{0.95}N$ Coating

XRD analysis on the $Ti_{0.05}Al_{0.95}N$ coating was performed in two steps. At first a coating powder was characterized in order to obtain information about the phases present in the coating. The XRD pattern in Figure 18 indicates the presence of a hexagonal AlN phase as well as cubic TiN and AlN phases.

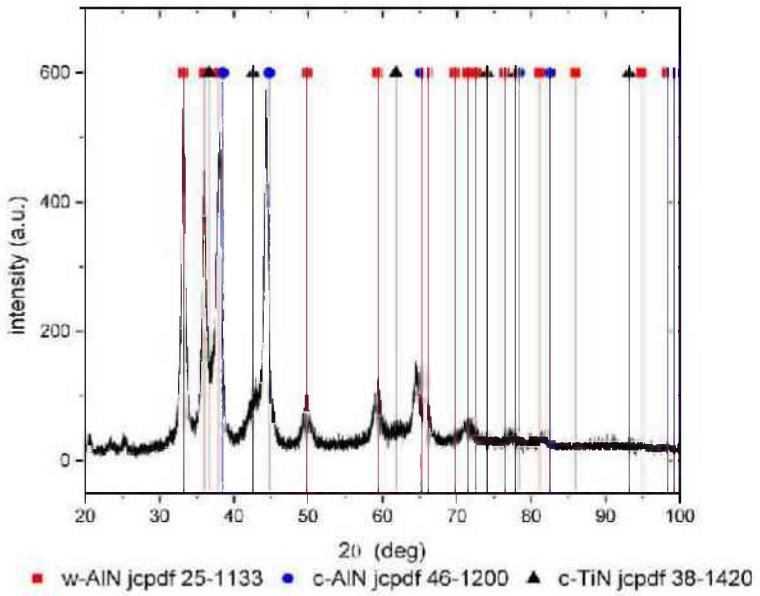

Figure 18. XRD data from $Ti_{0.05}Al_{0.95}N$ powder documents the presence of hexagonal AlN as well as cubic TiN and AlN phases. The vertical lines represent peak positions according to the ICDD powder diffraction database.

As a next step, the coatings deposited on the substrate were analysed. In Figure 19, diffraction data from the $Ti_{0.05}Al_{0.95}N$ coating indicate the presence of hexagonal AlN and cubic TiN and AlN phases, in agreement with the results measured from the powder produced from the same coating. Comparing the diffraction patterns from Figure 18 and Figure 19 indicate that there are some additional peaks in Figure 19, which can be attributed to diffraction from the substrate.

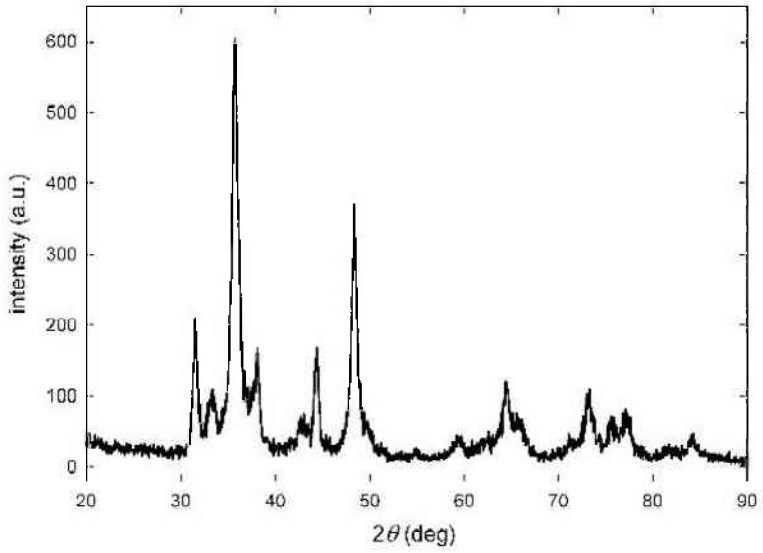

Figure 19. The XRD pattern from the $Ti_{0.05}Al_{0.95}N$ coating on the substrate indicate the presence of all reflections visible in Figure 16 as well as some additional reflections which can be attributed to the substrate.

4.1.2 XRD on $Ti_{0.2}Al_{0.8}N$ Coating

XRD analysis on the $Ti_{0.2}Al_{0.8}N$ coating was also performed in two steps. The powder diffraction pattern in Figure 20 indicates a presence of a face centred cubic (fcc) phase, which peak positions lie between cubic TiN and AlN peaks. There are no traces of hexagonal phase visible in the pattern.

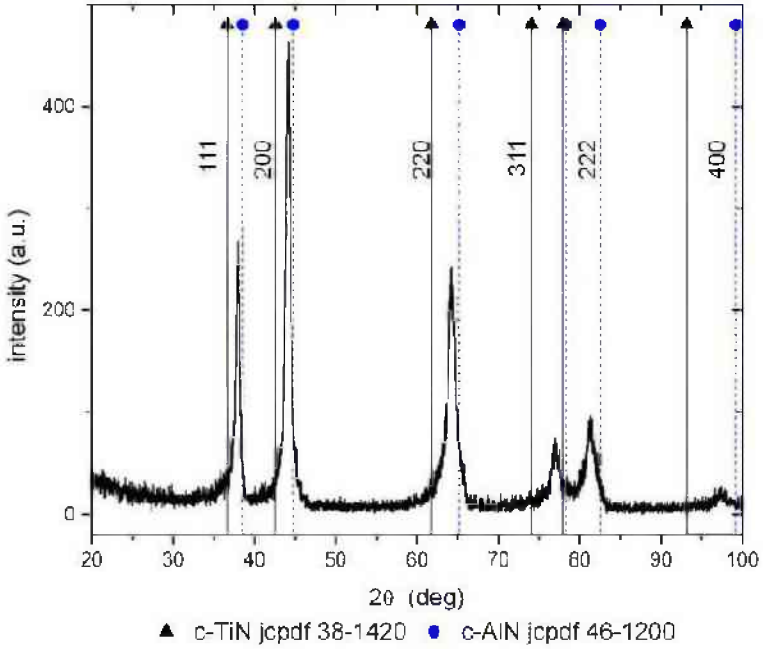

Figure 20. XRD data from $Ti_{0.2}Al_{0.8}N$ powder documents the presence of a fcc phase, with peaks between the peaks of cubic TiN and AlN phases. The vertical lines mark peak positions according to the ICDD powder diffraction database.

In Figure 21, a XRD pattern collected from $Ti_{0.2}Al_{0.8}N$ coating on the substrate is presented. In this case again the peaks from the fcc phase are visible. The comparison of the diffraction patterns from Figure 20 and Figure 21 indicate that there are some additional peaks in Figure 21, which can be attributed to the diffraction signal of the substrate.

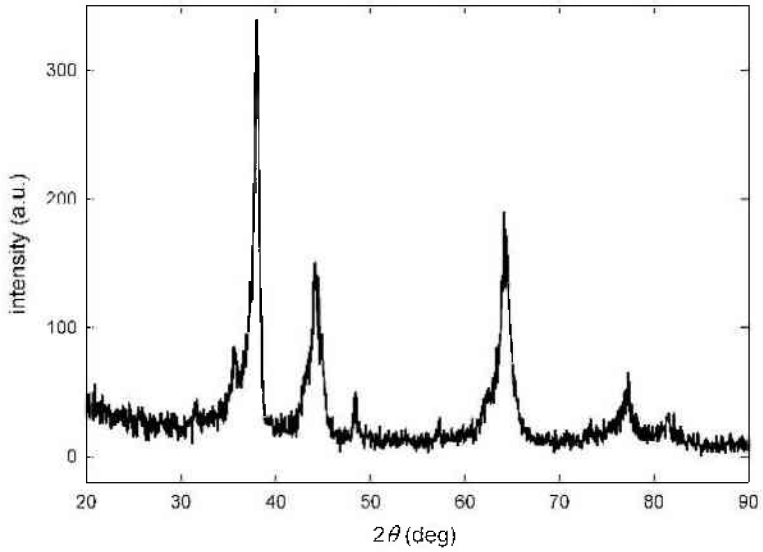

Figure 21. XRD data from $Ti_{0.2}Al_{0.8}N$ coating on the substrate indicate the presence of all fcc phase reflections visible also in Figure 18 as well as some additional reflections which can be attributed to the substrate.

4.1.3 XRD on $Ti_{1-x}Al_xN$ Multi-layered Nacre Coating

In Figure 22, a complex XRD pattern collected from the nacre coatings on the substrate is presented. The pattern indicates the presence of hexagonal AlN, cubic TiN and AlN, as well as substrate phases.

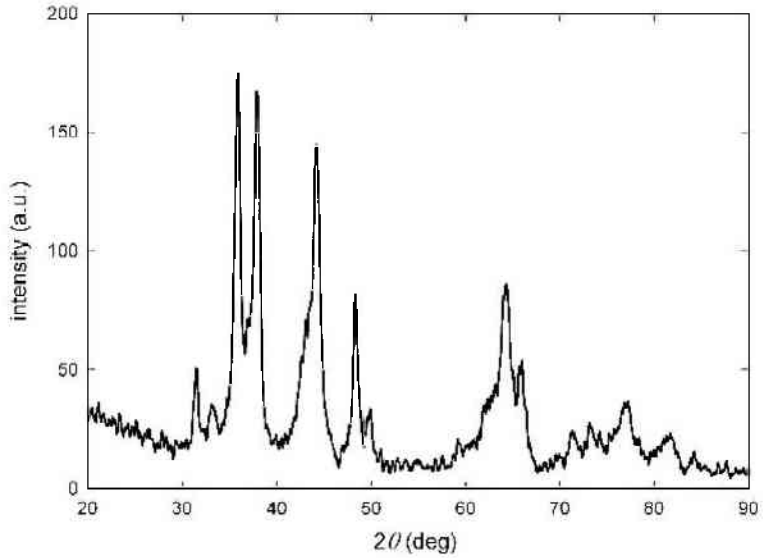

Figure 22. XRD data from the nacre coating on WC-Co substrate indicate the presence of all reflections visible in Figure 16 and 18 as well as some additional reflections which can be attributed to the substrate.

4.2 Microstructure Characterization using TEM

In this section the investigation of microstructure is outlined, beginning with the $Ti_{0.05}Al_{0.95}N$ coating, followed by the $Ti_{0.2}Al_{0.8}N$ coating and the multi-layered $Ti_{1-x}Al_xN$ nacre-like coating. The images presented in the following section were collected using STEM and HR-TEM.

4.2.1 $Ti_{0.05}Al_{0.95}N$ Coating Microstructure

Figure 23 shows a high-angle annular dark-field (HAADF)-micrograph collected from the $Ti_{0.05}Al_{0.95}N$ coating with characteristic self-organized cubes formed during the deposition process. By analysing the Z-contrast of the image, the higher Ti-content in the brighter regions of Figure 23 was identified. The self-organized cubes are surrounded by the fcc-$Ti_{1-x}Al_xN$ matrix.

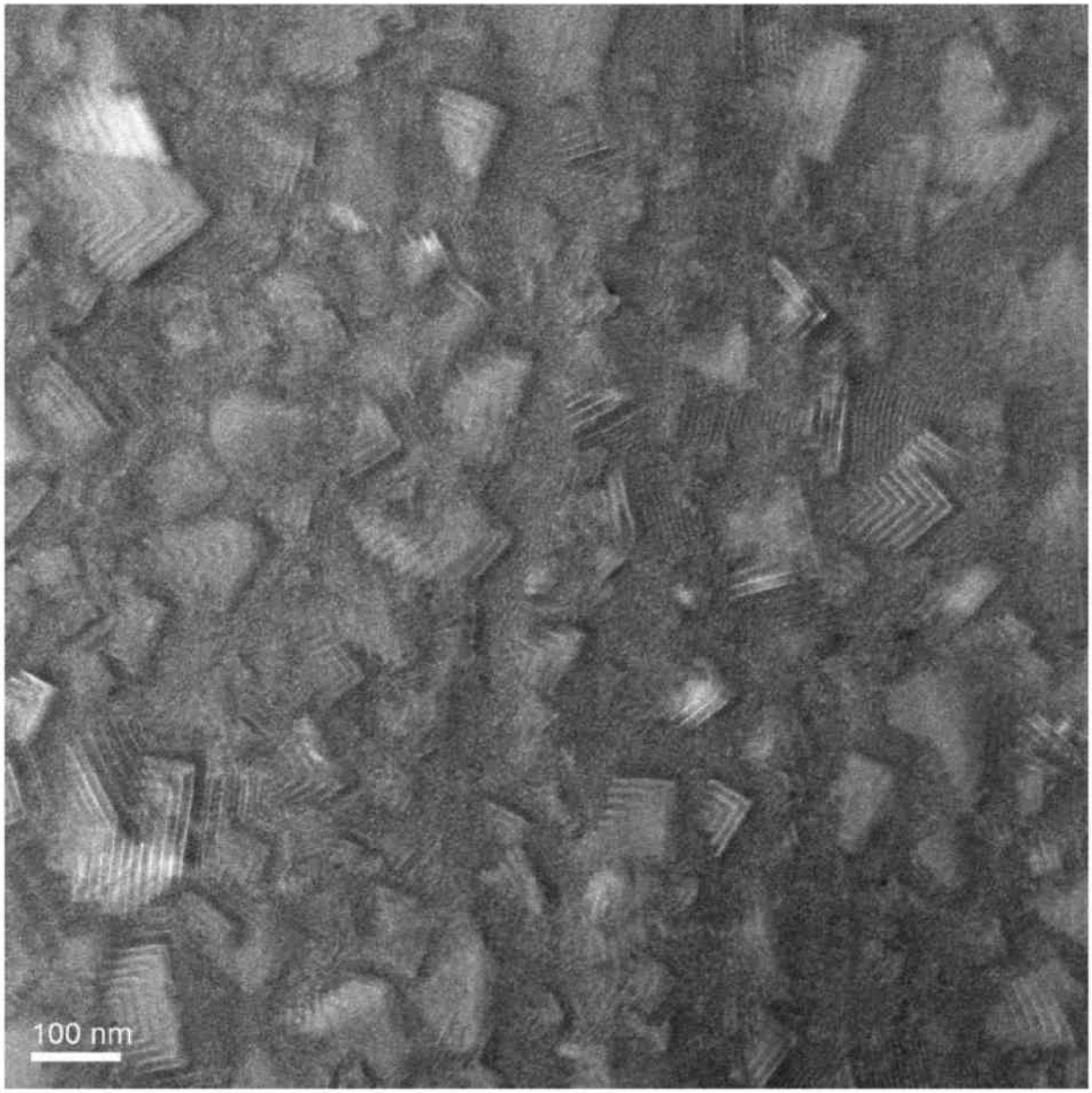

Figure 23. HAADF-STEM micrograph of the $Ti_{0.05}Al_{0.95}N$-coating indicating the presence of a self-organized nanolamellar microstructure in the coating

Figure 24 shows a high resolution image of the sample, where the alterating incoherent lamellae of w-AlN and c-TiN can be identified. The thickness of TiN nanolamellae is ~3 nm, the overall layer periodicity is ~13 nm.

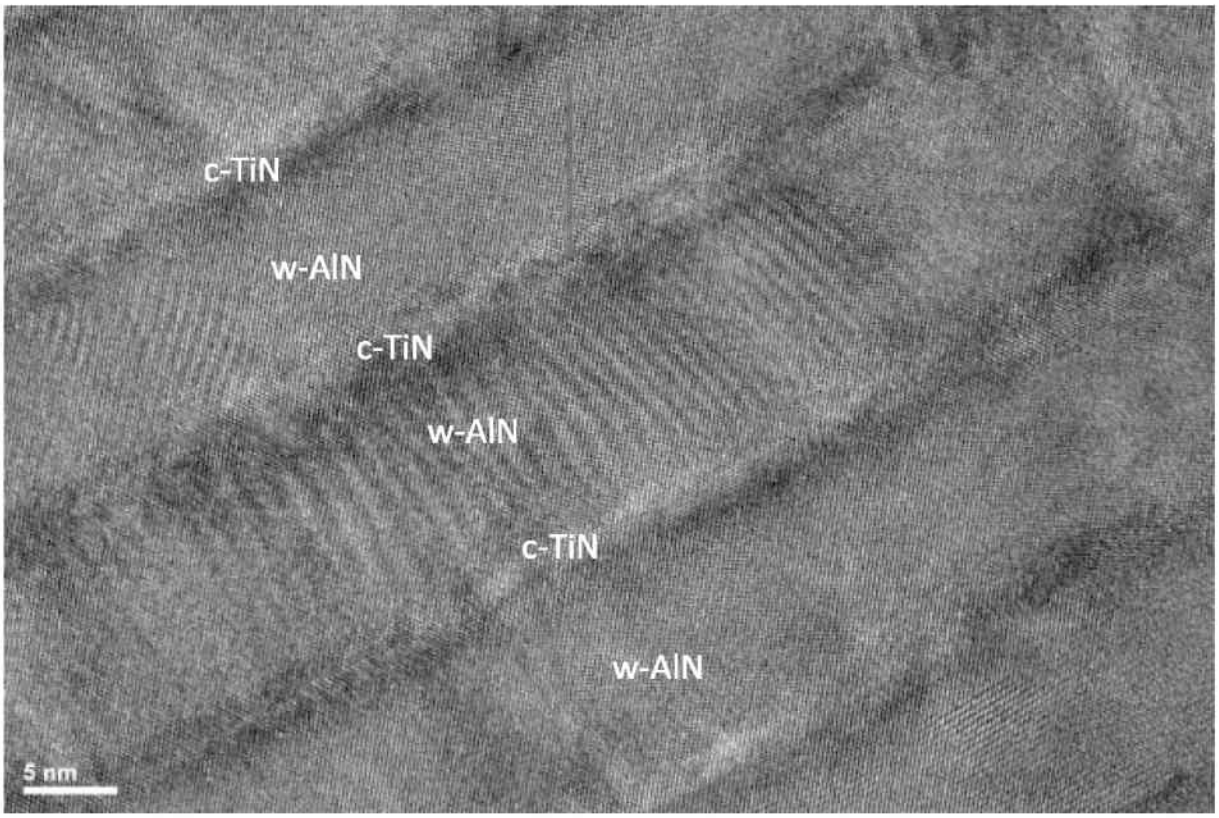

Figure 24. HR-TEM image of the self-organized incoherent w-AlN and c-TiN nanolamellae within the $Ti_{0.05}Al_{0.95}N$ coating

4.2.2 $Ti_{0.2}Al_{0.8}N$ Coating Microstructure

Figure 25 shows a HAADF micrograph of the $Ti_{0.2}Al_{0.8}N$ coating where the nanolamellar structure can be seen in detail. The bright lines in the image represent the regions with high Ti-content of relatively high Z-contrast.

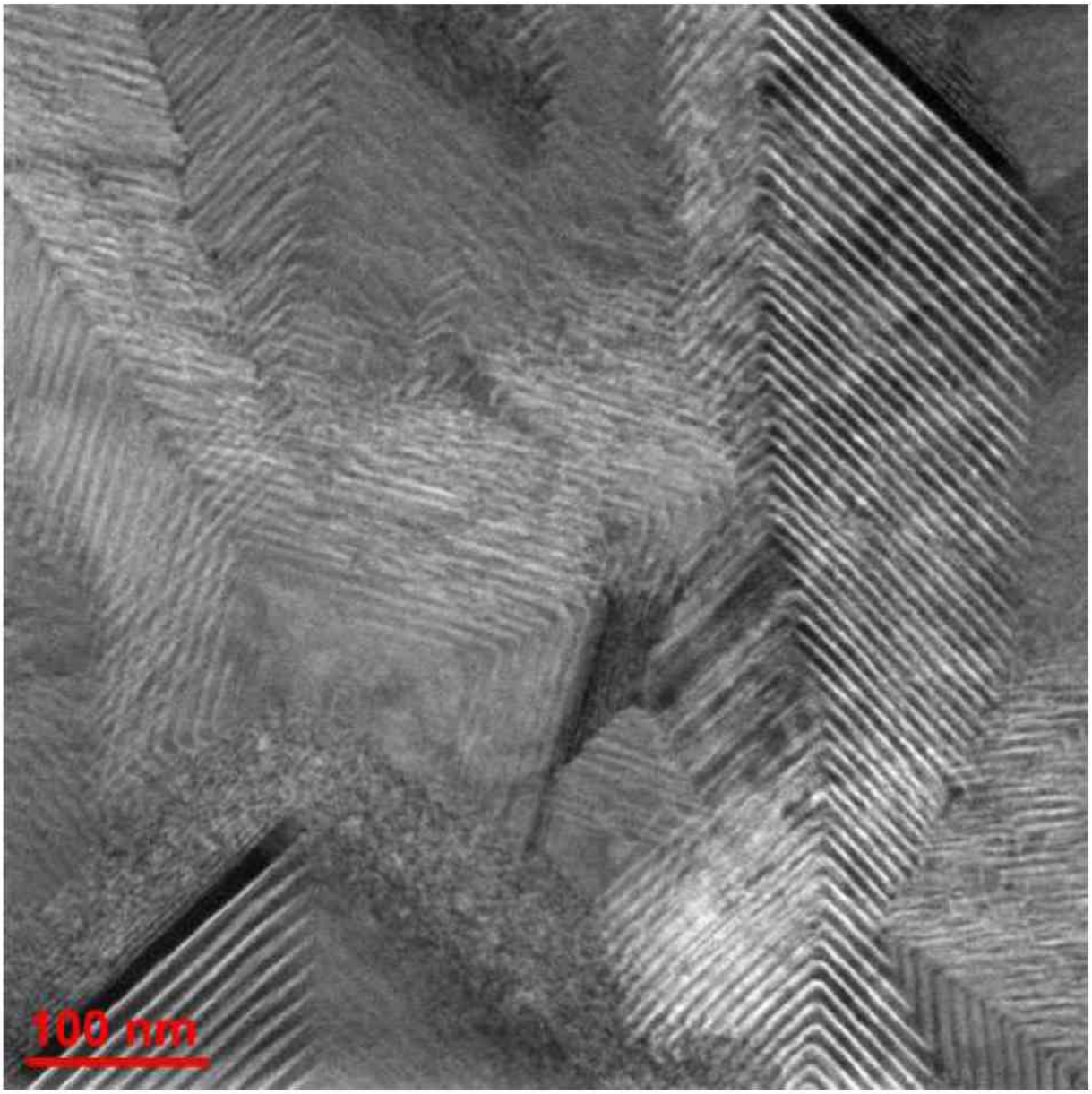

Figure 25. HAADF-STEM micrograph of the $Ti_{0.2}Al_{0.8}N$ coating with nanolamellar microstructure

In Figure 26, a detailed high-resolution TEM micrograph is presented, in which it is possible to recognize some sort of epitaxial relationship between the fcc-TiN and the fcc-AlN nanolamellae. It also shows that the lamellae are coherent. The thickness of the individual TiN nanolamellae sublayers is ~1.3 nm, while the thickness of the AlN nanolamellae is in the range of ~10 nm.

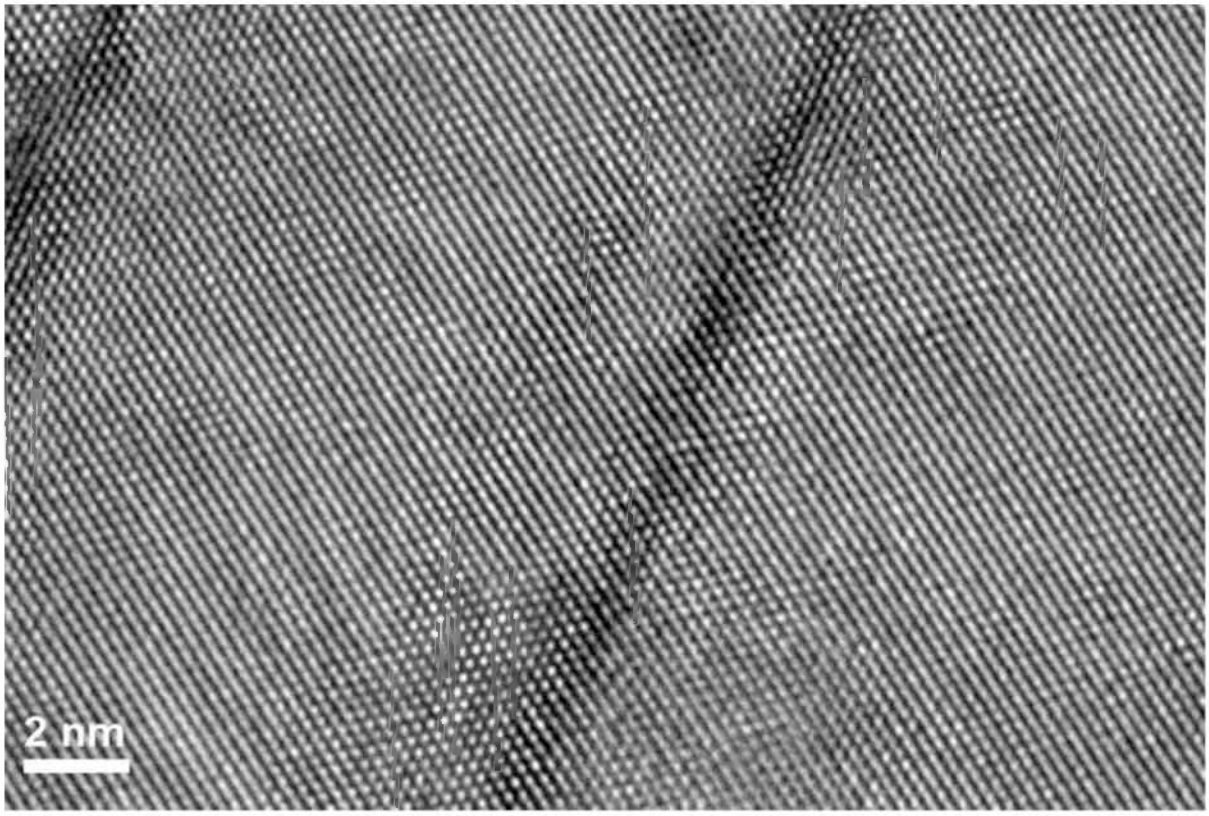

Figure 26. High-resolution image of the TiN-AlN interface demonstrating the presence of coherent nanolamellar microstructure.

4.2.3 $Ti_{1-x}Al_xN$ Multi-layered Coating

The HAADF micrograph in Figure 27 below confirms that the coating is indeed composed of the two structures described above. The bright regions represent cubic $Ti_{0.2}Al_{0.8}N$ sublayers of about 0.5µm thickness, whereby the relatively dark regions in between show interlayers of $Ti_{0.05}Al_{0.95}N$ that are only about 50nm thick. Since the volume fraction of Ti in the thick lamellae is higher, these appear much brighter in Figure 27. Due to the varying surface growth kinetics, the interfaces between the lamellae show wave-like morphology, especially towards the surface. Since the $Ti_{0.2}Al_{0.8}N$ sublayers possess a higher hardness compared to their $Ti_{0.05}Al_{0.95}N$ counterparts, the multi-layered coating shown in Figure 27 will henceforth be denoted as **$Ti_{1-x}Al_xN$ nacre** coating.

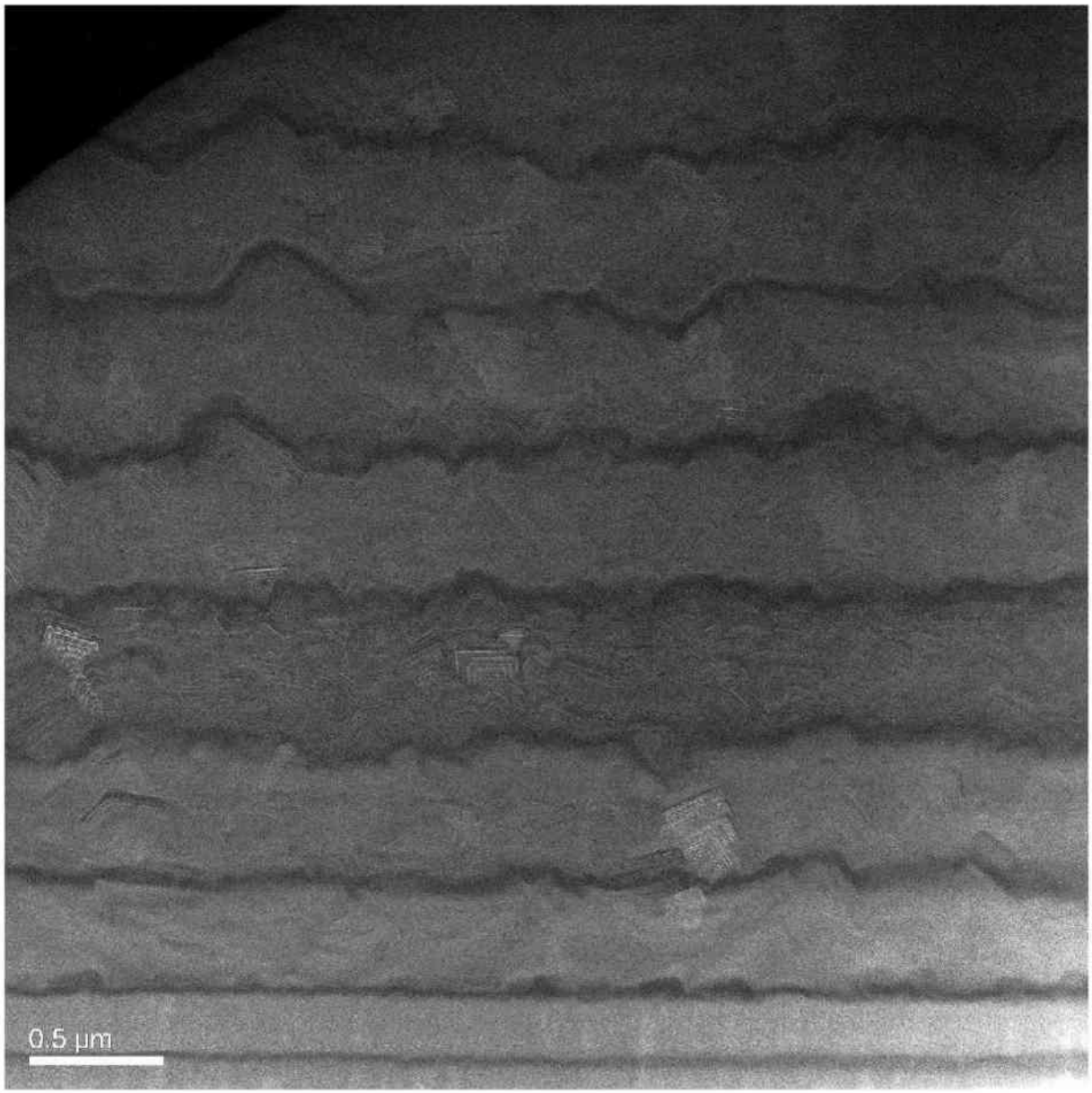

Figure 27. HAADF-STEM micrograph of the multi-layered $Ti_{1-x}Al_xN$ nacre coating, which thick and thin sublayers consist of alternating $Ti_{0.2}Al_{0.8}N$ and $Ti_{0.05}Al_{0.95}N$, respectively

4.3 Hardness and Indentation Modulus Characterization

As discussed in chapters 2.4 and 3.6, hardness and indentation modulus were determined using the Oliver-Pharr Method [47]. For the $Ti_{0.05}Al_{0.95}N$ coating, hardness and indentation modulus of 26.1±1.1 GPa and 356±15.4 GPa, respectively, were evaluated and reported by Todt *et. al.* in 2014 [24].

The indentation experiments on the $Ti_{0.2}Al_{0.8}N$ coating were done in a series of 15 indents varying the force gradually from 14 to 25 mN. Figure 28 shows the load-indentation depth curves obtained during the experiments. The evaluation led to hardness value of 36.1±1.8 GPa, which was already reported by Todt *et. al.* in 2016 [25], and indentation modulus of 522±16 GPa.

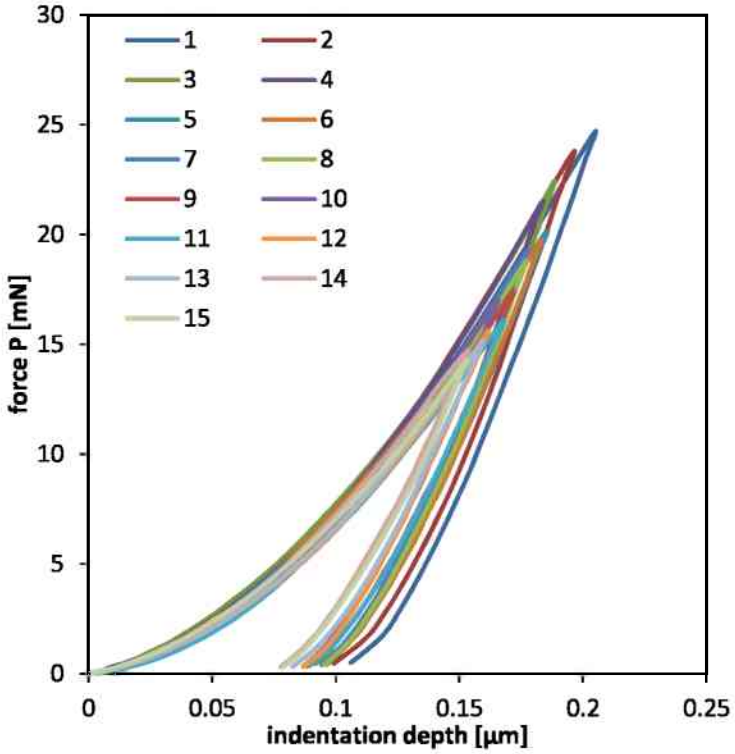

Figure 28. Load-indentation depth curves measured during indentation experiments on $Ti_{0.2}Al_{0.8}N$ coating.

Indentation experiments were also performed on the multi-layered $Ti_{1-x}Al_xN$ nacre coating. Figure 29 shows examples of load-indentation depth curves for a series of 14 individual indents. The force was varied gradually from 15 to 30 mN.

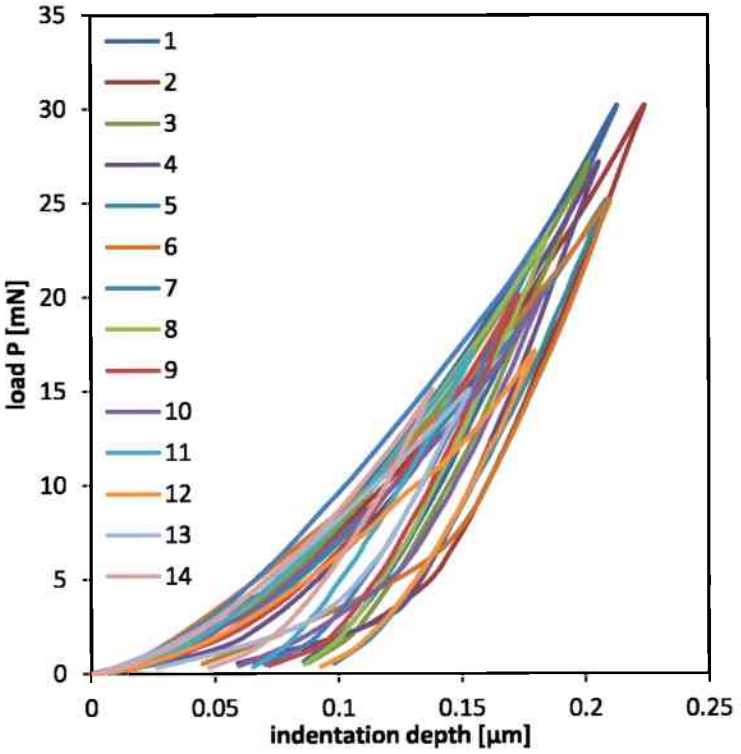

Figure 29. Load-indentation depth curves measured during indentation experiments on $Ti_{1-x}Al_xN$ nacre coating.

Figure 30 shows the evaluated hardness and indentation modulus for each indent. The average hardness was determined to be 30.7±4.3 GPa, while the average indentation modulus was 447±42 GPa. The scattering of the measured values and the relatively large measurements errors can be explained by the comparatively high coating roughness, which affected the indentation experiments to some degree.

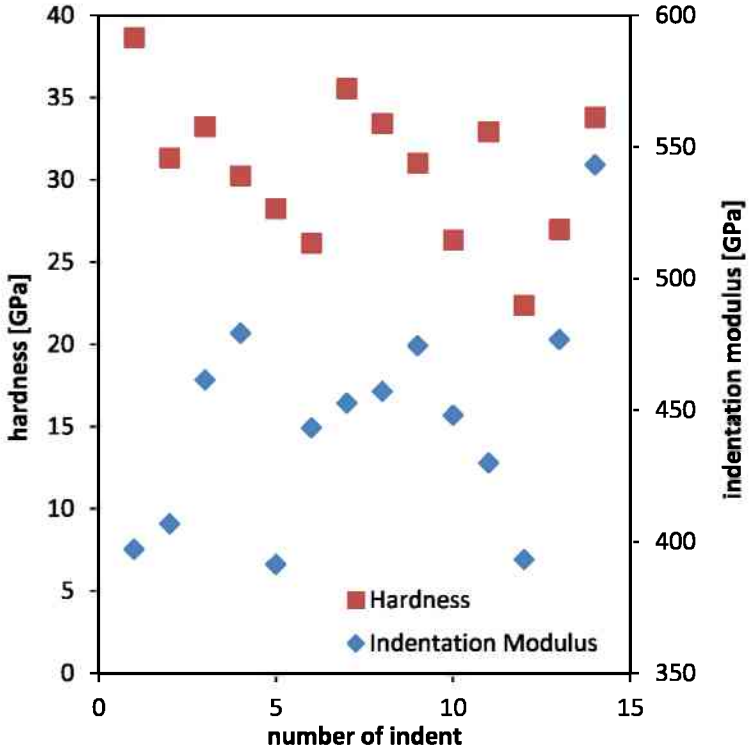

Figure 30. Hardness and indentation modulus determined from individual indentation experiments on $Ti_{1-x}Al_xN$ nacre coating.

4.4 Micro-Cantilever Bending Experiments

In this section, results from bending experiments on un-notched cantilevers are presented, together with measured experimental stress-strain dependencies. Table 1 lists the cantilever geometry for every tested cantilever, as well as the orientation in which the cantilever was loaded. In this experimental setup the cantilevers were not notched, and the purpose was the evaluation of Young's modulus and fracture stress.

For the in-plane orientation, (IP) in Table 1, the bending direction is parallel to the substrate-coating interface (Figure 6). In the out-of-plane orientation, (OoP) in Table 1, the bending direction is normal to the substrate-coating interface (Figure 5).

Table 1. Geometry of the un-notched cantilevers used for the determination of Young's modulus and fracture stress on three different coating types in in-plane (IP) and out-of-plane (OoP) testing orientations.

coating	cantilever no.	orientation	length *L* [µm]	width *B* [µm]	thickness *t* [µm]
$Ti_{1-x}Al_xN$ nacre	1	OoP	9.80	2.17	2.35
$Ti_{1-x}Al_xN$ nacre	2	OoP	9.38	1.99	2.22
$Ti_{1-x}Al_xN$ nacre	3	IP	9.05	2.32	2.12
$Ti_{1-x}Al_xN$ nacre	4	IP	9.09	2.46	2.14
$Ti_{0.2}Al_{0.8}N$	1	OoP	10.00	2.37	1.78
$Ti_{0.2}Al_{0.8}N$	2	OoP	10.20	2.10	2.26
$Ti_{0.2}Al_{0.8}N$	3	IP	9.16	2.278	2.00
$Ti_{0.05}Al_{0.95}N$	1	OoP	9.60	2.17	2.11
$Ti_{0.05}Al_{0.95}N$	2	OoP	9.63	2.15	2.17
$Ti_{0.05}Al_{0.95}N$	3	IP	9.38	2.14	2.21
$Ti_{0.05}Al_{0.95}N$	4	IP	9.26	2.14	2.19
$Ti_{0.05}Al_{0.95}N$	5	IP	9.38	2.07	2.19

4.4.1 Fracture Stress and Young's Modulus of $Ti_{0.05}Al_{0.95}N$ Coating

The load-displacement data which were collected during the bending experiments were transformed into stress-strain data using Eqs. 41 and 44. Figure 31 shows the stress-strain curves collected from the $Ti_{0.05}Al_{0.95}N$ coating. Cantilevers 1-3 were tested in out-of-plane and cantilevers 4-5 in-plane testing geometry, respectively. The observed stress-strain behaviour in Figure 31 indicates the absence of mechanical anisotropy within the coating.

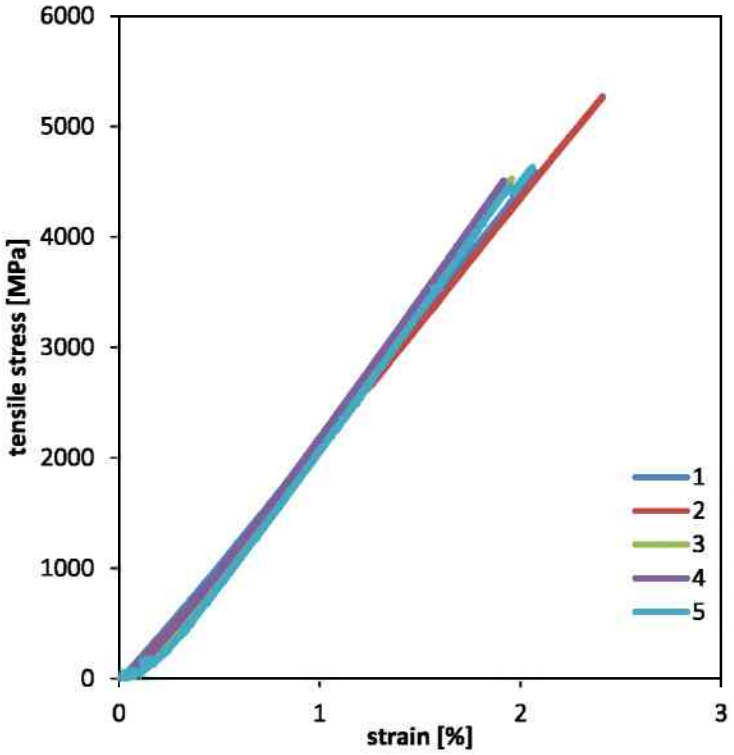

Figure 31. Stress-strain curves collected from bending experiments on un-notched $Ti_{0.05}Al_{0.95}N$ cantilevers

Young's modulus and fracture stress were evaluated separately for in-plane and out-of-plane loading directions and are presented Table 2.

Table 2. Mechanical properties of the $Ti_{0.05}Al_{0.95}N$ coating evaluated from bending tests on un-notched cantilevers

	Young's modulus [GPa]	fracture stress [GPa]
out-of-plane	224±4	4.9±0.5
in-plane	236±3	4.6±0.1

4.4.2 Fracture Stress and Young's Modulus of $Ti_{0.2}Al_{0.8}N$ Coating

The load-displacement data, which were collected during the bending experiments on $Ti_{0.2}Al_{0.8}N$ micro-cantilevers, were transformed into stress-strain data using Eqs. 41 and 44. Figure 32 shows stress-strain curves. Cantilevers 1 and 2 were rested in out-of-plane geometry and the cantilever 3 was fractured in in-plane orientation. No pronounced anisotropy was found for the Young's modulus, whereas anisotropic fracture behaviour was detected (Figure 32).

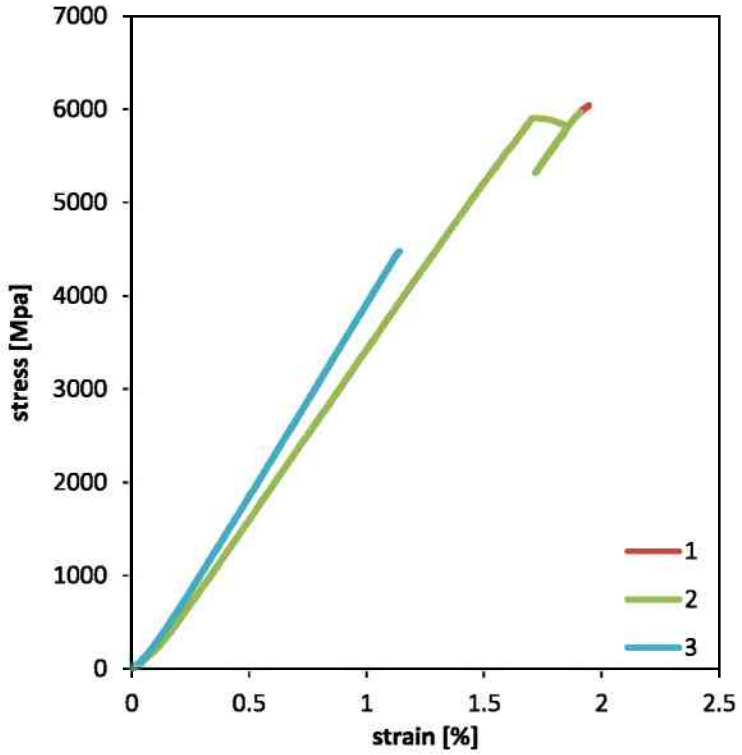

Figure 32. Stress-strain curves collected during bending experiments on un-notched $Ti_{0.2}Al_{0.8}N$ cantilevers. The data from the micro-cantilevers 1 and 2 are practically identical.

The value for Young's modulus was separately evaluated for in-plane and out-of-plane orientation, as has been done for the fracture stress. Table 3 shows the evaluated mechanical properties.

Table 3. Mechanical properties of $Ti_{0.2}Al_{0.8}N$ evaluated from bending tests on un-notched cantilevers.

	Young's modulus [GPa]	fracture stress [GPa]
out-of-plane	383±19	5.7±0.5
in-plane	407	4.5

4.4.3 Fracture Stress and Young's Modulus of $Ti_{1-x}Al_xN$ Nacre Coating

The load-displacement data which were collected during the bending experiments were transformed into stress-strain curves using Eqs. 41 and 44. Figure 33 shows the stress-strain curves for the $Ti_{1-x}Al_xN$ nacre coating. Cantilevers 1 and 2 were tested in out-of-plane orientation and cantilevers 3 and 4 were dedicated to in-plane testing. A slight anisotropy was detected during the in-plane and the out-of-plane testing for the Young's modulus and fracture stress.

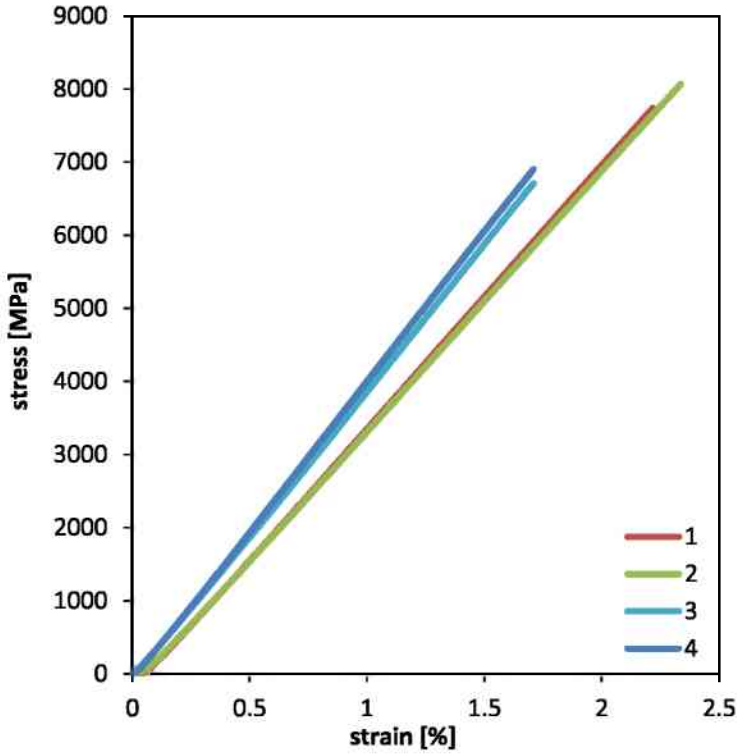

Figure 33. Stress-strain curves collected during bending experiments on un-notched $Ti_{1-x}Al_xN$ nacre cantilevers.

The Young's modulus was separately evaluated for in-plane and out-of-plane orientation, the same has been done for the fracture stress. Table 4 shows the evaluated mechanical properties.

Table 4. Mechanical properties of $Ti_{1-x}Al_xN$ nacre coating evaluated from bending tests on un-notched cantilevers.

	Young's modulus [GPa]	fracture stress [GPa]
out-of-plane	355±7	7.9±0.2
in-plane	385±26	6.3±0.6

4.5 Fracture Toughness Experiments

In this section, results from bending experiments on notched cantilevers are presented, together with the experimental dependencies of stress intensity–normalized strain at notch. In Table 5 the cantilever geometry is listed for each cantilever, as well as the testing geometry in which the cantilever was loaded.

Since the cantilevers were notched, the purpose was the evaluation of fracture toughness K_{Ic}. For the in-plane orientation (Figure 5), later named as IP, the bending direction is parallel to the substrate-coating interface. In the out-of-plane orientation (Figure 6), further denoted as OoP, the bending direction is normal to the substrate-coating interface. The notch depth a was measured ex-situ in the ZEISS LEO 1525 SEM by analysing the cross-sections of the broken cantilevers.

Table 5. Geometry of the notched cantilever used for fracture toughness characterization on three different coating types in in-plane (IP) and out-of-plane (OoP) orientations

coating	cantilever no.	orientation	length L [µm]	width B [µm]	thickness t [µm]	notch depth a [µm]
$Ti_{1-x}Al_xN$ nacre	1	OoP	8.31	2.17	2.3	0.378
$Ti_{1-x}Al_xN$ nacre	2	OoP	8.49	2.21	2.41	0.417
$Ti_{1-x}Al_xN$ nacre	3	OoP	8.46	2.14	2.37	0.434
$Ti_{1-x}Al_xN$ nacre	4	OoP	8.46	2.14	2.35	0.389
$Ti_{1-x}Al_xN$ nacre	5	IP	8.00	2.35	2.22	0.829
$Ti_{1-x}Al_xN$ nacre	6	IP	8.08	2.30	2.26	0.885
$Ti_{0.2}Al_{0.8}N$	1	OoP	7.99	1.72	2.39	0.281
$Ti_{0.2}Al_{0.8}N$	2	IP	6.12	2.22	1.78	0.638
$Ti_{0.2}Al_{0.8}N$	3	IP	7.43	2.1	2.24	0.350
$Ti_{0.05}Al_{0.95}N$	1	OoP	8.1	2.03	2.22	0.462
$Ti_{0.05}Al_{0.95}N$	2	OoP	7.88	2.17	2.24	0.434
$Ti_{0.05}Al_{0.95}N$	3	OoP	8.15	2.09	2.22	0.557
$Ti_{0.05}Al_{0.95}N$	4	IP	7.35	2.13	2.24	0.542
$Ti_{0.05}Al_{0.95}N$	5	IP	7.38	2.19	2.16	0.502
$Ti_{0.05}Al_{0.95}N$	6	IP	7.54	2.16	2.16	0.521

4.5.1 Fracture Toughness of $Ti_{0.05}Al_{0.95}N$ Coating

The load-displacement data which were collected during the bending experiments were transformed into stress intensity-strain at notch using Eqs. 53 and 44. Figure 34 shows the experimental curves of stress intensity-strain at notch for the $Ti_{0.05}Al_{0.95}N$ coating. Cantilevers 1-3 and 4-6 were tested in in-plane and out-of-plane orientations, respectively. Average values of fracture toughness were separately evaluated for both orientations, which resulted in 3.1±0.1 $MPam^{½}$ for in-plane measurements, and 3.1±0.2 $MPam^{½}$ in the out-of-plane case. The evaluated toughness values indicate an absence of fracture toughness anisotropy.

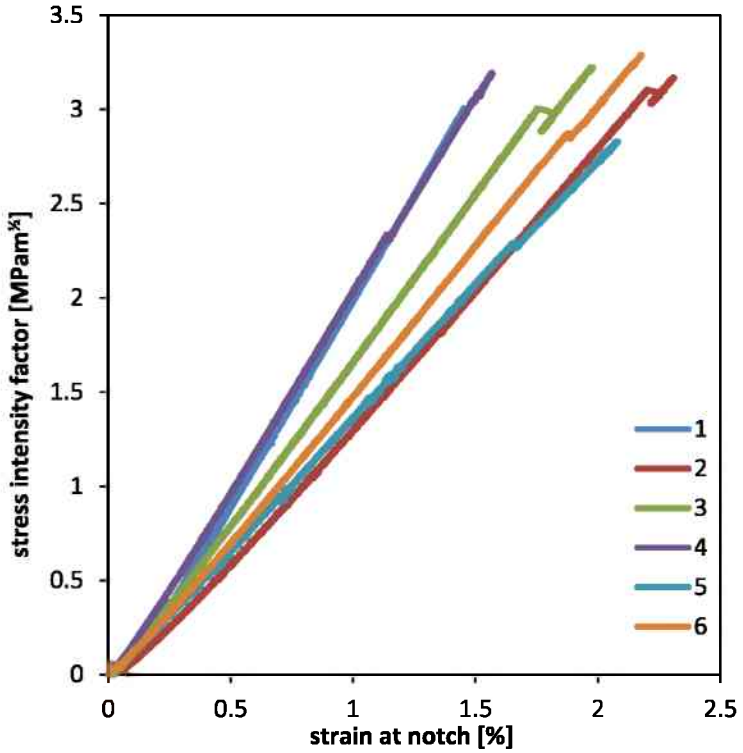

Figure 34. Stress intensity-strain curves collected during bending experiments on $Ti_{0.05}Al_{0.95}N$ cantilevers. Cantilevers 1-3 and 4-6 were tested in in-plane and out-of-plane orientations, respectively.

4.5.2 Fracture Toughness of $Ti_{0.2}Al_{0.8}N$ Coating

The load-displacement data which were collected during the bending experiments were transformed into stress intensity-strain dependencies using Eqs. 53 and 44. Figure 35 shows the experimental curves of stress intensity-strain at the notch for the $Ti_{0.2}Al_{0.8}N$ coating. Here Cantilever 1 was tested in out-of-plane orientation whereas cantilevers 2 and 3 were fractured in in-plane orientation. The fracture toughness was separately evaluated for in-plane and out-of-plane sample orientation and found to be 5.0±0.4 and 5.4 $MPam^{½}$, respectively.

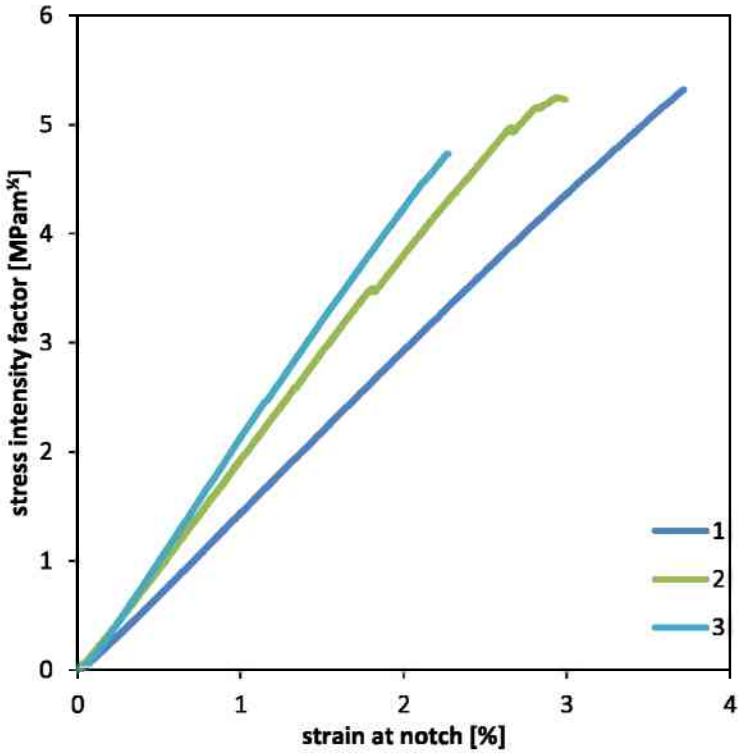

Figure 35. Stress intensity-strain curves collected during bending experiments on notched $Ti_{0.2}Al_{0.8}N$ cantilevers. Cantilevers 1 and 2, 3 were tested in out-of-plane orientation and in in-plane orientation, respectively.

4.5.3 Fracture Toughness of $Ti_{1-x}Al_xN$ Nacre Coating

The load-displacement data which were collected during the bending experiments were transformed into stress intensity-strain dependencies at notch using Eqs. 53 and 44. Figure 36 shows the experimental curves of stress intensity-strain at notch for the $Ti_{1-x}Al_xN$ nacre coating. Cantilevers 1-4 were tested in out-of-plane orientation and cantilevers 5 and 6 were fractured in in-plane orientation.

The results were used to evaluate average fracture toughness values in-plane and out-of-plane orientations with 4.2±0.6 $MPam^{½}$ and 4.7±0.4 $MPam^{½}$, respectively.

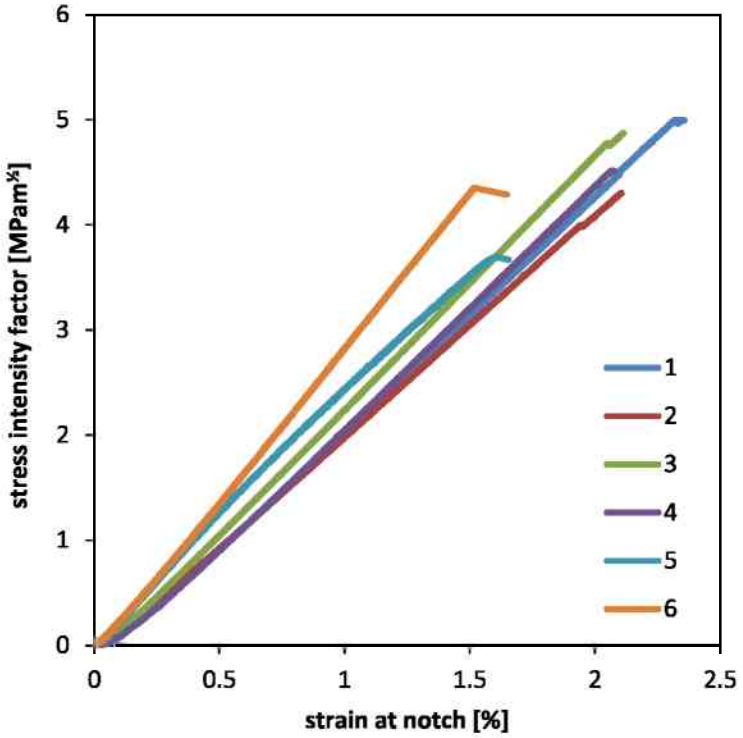

Figure 36. Stress intensity-strain curves collected during bending experiments on notched $Ti_{1-x}Al_xN$ nacre cantilevers. Cantilever 1-4 and 5-6 were tested in out-of-plane and in-plane orientation, respectively.

5. Discussion

In this chapter, the quantitative experimental results collected during micro-mechanical experiments will be discussed and related to the coatings microstructure as well as to the morphologies of the cantilever fracture surfaces.

5.1 Young's Modulus Variation

The Young's modulus of AlN strongly depends on the crystal structure as it has been shown by Christensen and Gorczyca in 1993 [21]. The phase transition was reached by applying a pressure of approximately 12.5 GPa to the AlN and resulted in a shift of Young's modulus from 205 GPa for the wurtzite phase to approximately 400 GPa for the rocksalt structure. The observed difference in Young's modulus of roughly 160 GPa between $Ti_{0.05}Al_{0.95}N$ (Table 2) and $Ti_{0.2}Al_{0.8}N$ (Table 3) can be explained by the presence of different AlN polytypes in the respective coatings. In the $Ti_{0.2}Al_{0.8}N$ coating the cubic AlN phase was stabilized not by the external pressure, but by the cubic TiN nanolamellae.

For the $Ti_{1-x}Al_xN$ nacre coating the modulus of 355 GPa for out-of-plane orientation and 385 GPa for in-plane orientation (Table 4) is slightly smaller than that of the pure $Ti_{0.2}Al_{0.8}N$ coating, which can be attributed to the smaller volume fraction of wurtzite $Ti_{0.05}Al_{0.95}N$ phase.

5.1.1 Anisotropy of Young's Modulus

For the $Ti_{0.05}Al_{0.95}N$ coating, no anisotropy in the modulus with respect to the testing direction was detected. This observation is in agreement with the coating microstructure shown in the STEM-HAADF micrograph (Figure 23). The self-organized crystallites are randomly distributed, no texture can be identified and therefore the observed isotropic material elastic response is reasonable.

A similar behaviour was observed in the case of the $Ti_{0.2}Al_{0.8}N$ coating. This can be related to the coating microstructure, which is composed of crystallites irregularly faceted and which form a herringbone pattern within the self-organized layers. These crystallites are randomly oriented. (cf. Figure 25).

For the $Ti_{1-x}Al_xN$ nacre coating, a small anisotropy was found for the Young's modulus by comparing the values for in-plane and out-of-plane direction (cf. Table 4).

For the tested samples there is no sharp interface between the individual $Ti_{1-x}Al_xN$ phases, so typical models, like the rule-of-mixture approach, do only apply only partially here.

In Figure 37 the loading geometry and the stress distribution for an in-plane loaded cantilever are schematically shown.

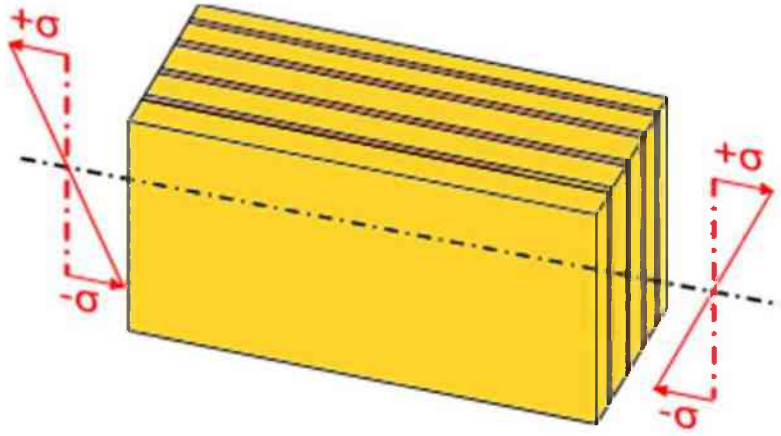

Figure 37. A schematic distribution of stresses in in-plane loaded multi-layered cantilever.

The Young's modulus over the phase content x of $Ti_{0.2}Al_{0.8}N$ coating for the in-plane orientation, according to the model is

$$E_{\text{in-plane}} = (1-x) \times E_{Ti_{0.05}Al_{0.95}N} + x \times E_{Ti_{0.2}Al_{0.8}N} \quad (56)$$

In Figure 38 the loading state and the stress distribution for an out-of-plane loaded cantilever are shown.

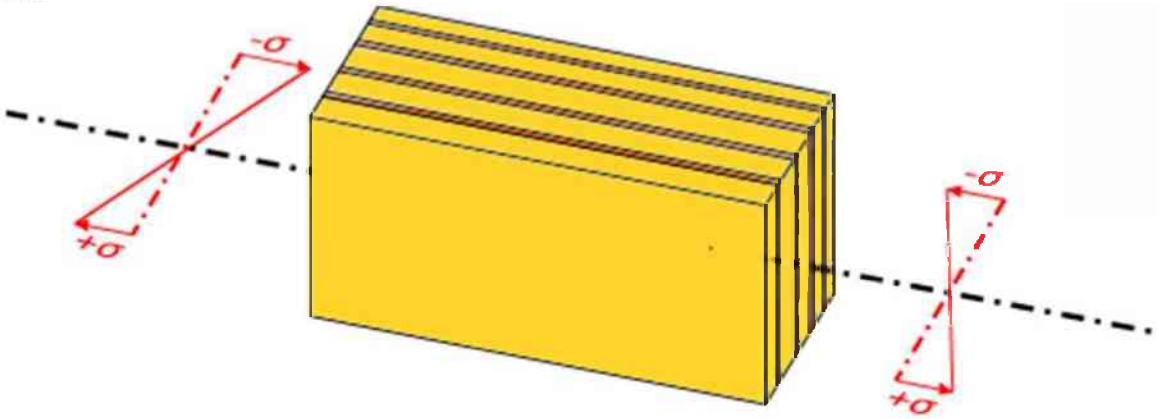

Figure 38. A schematic distribution of stresses in out-of-plane loaded cantilever

The corresponding Young's modulus for the out-of-plane orientation is calculated using

$$\frac{1}{E_{\text{out-of-plane}}} = \frac{(1-x)}{E_{Ti_{0.05}Al_{0.95}N}} + \frac{x}{E_{Ti_{0.2}Al_{0.8}N}}. \quad (57)$$

Figure 39 shows the calculated theoretical rule-of-mixture moduli for in-plane and out-of-plane orientations. The Young's modulus is plotted against the $Ti_{0.2}Al_{0.8}N$ phase content, where zero stands for the $Ti_{0.05}Al_{0.95}N$ coating and one for the $Ti_{0.2}Al_{0.8}N$ coating. The ideal behaviour is outlined by the curves in the graph for in-plane (blue) and out-of-plane (red) orientation. The experimental values shown in Figure 39 relate to a $Ti_{0.2}Al_{0.8}N$ content of ~10/11, which can be calculated from the relative thicknesses of the sublayers (cf. Figure 27). Even if the rule-of-mixture does not apply exactly in the case of $Ti_{1-x}Al_xN$ nacre coating, the results fit very well with the predicted dependencies in Figure 39.

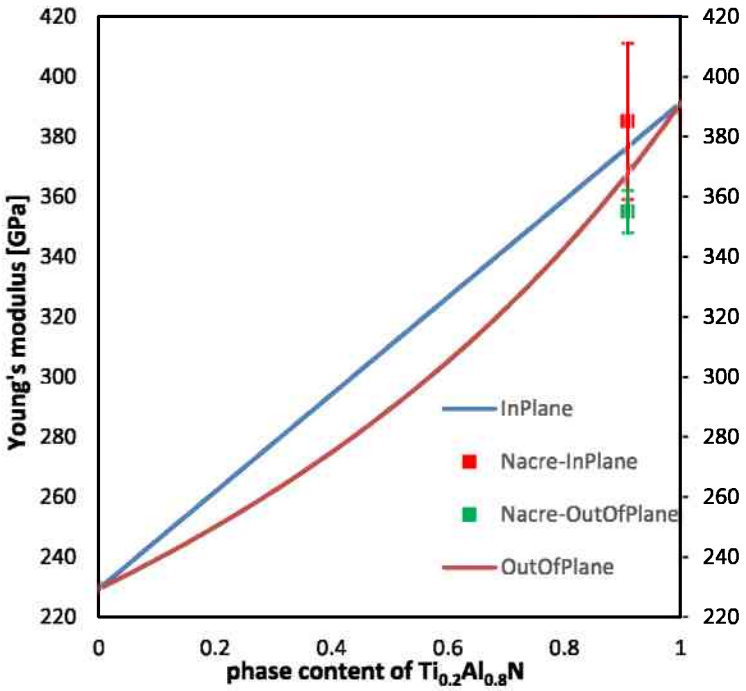

Figure 39 Theoretical out-of-plane and in-plane moduli compared to the measured values in the nacre coating with a $Ti_{0.2}Al_{0.8}N$ phase content of ~10/11.

5.2 Fracture Stress

In the following section the fracture behaviour of un-notched cantilevers, mainly the fracture stress will be discussed.

5.2.1 Fracture Stress of $Ti_{0.05}Al_{0.95}N$ Coating

The $Ti_{0.05}Al_{0.95}N$ coating showed the lowest fracture strength, exhibiting 4.6 GPa for in-plane and 4.9 GPa for out-of-plane orientation. The difference between the orientations is not significant, as it is in the case of Young's modulus. The fracture surfaces for out-of-plane and in-plane orientation are given in Figure 40. The fracture surfaces are relatively flat; the roughness is relatively small due to the size of the self-organized crystals, which is also quite small. The fracture surface roughness also indicates, compared to the microstructure from cf. Figure 23, that the fracture occurs between the self-organized crystallites. It means there is an intergranular fracture during the crack growth in the $Ti_{0.05}Al_{0.95}N$ coating.

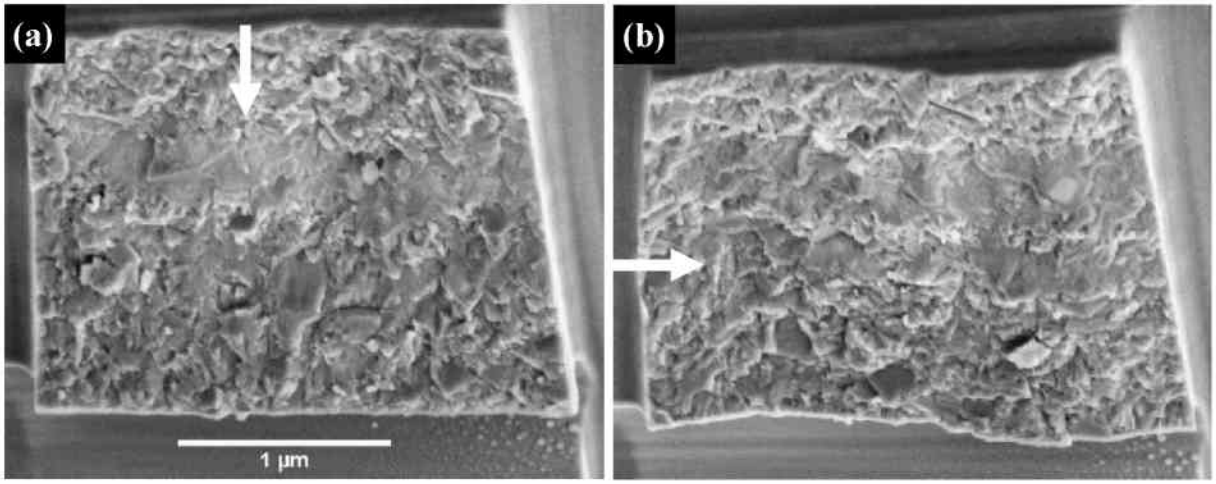

Figure 40. Fracture surface of un-notched $Ti_{0.05}Al_{0.95}N$ cantilevers tested in out-of-plane (a) and in-plane (b) geometry with arrows indicating the loading direction.

5.2.2 Fracture Stress of $Ti_{0.2}Al_{0.8}N$ Coating

The $Ti_{0.2}Al_{0.8}N$ coating exhibits higher values of fracture strength than its $Ti_{0.05}Al_{0.95}N$ counterpart. This is true in particular for the out-of-plane orientation where the fracture stress reaches 5.7 GPa. Figure 41 shows the related fracture surfaces of two un-notched cantilevers.

The fracture surfaces document that the fracture occurs at grain boundaries between the self-organized crystals (Figure 41). The enhancement of the fracture strength measured in out-of-plane testing orientation can be explained by a zig-zag shape of the fracture line in the outer fibre as well as by morphologically complex fracture surface. The fracture toughness enhancement originates from the repeated crack deflection which results in the consumption of crack energy when generating the large crack surface. This behaviour is not identical for the in-plane testing orientation, where the fracture line along the outer fibre is quite straight (Figure 41 b). Therefore the observed fracture stress is not as high as in out-of-plane orientation.

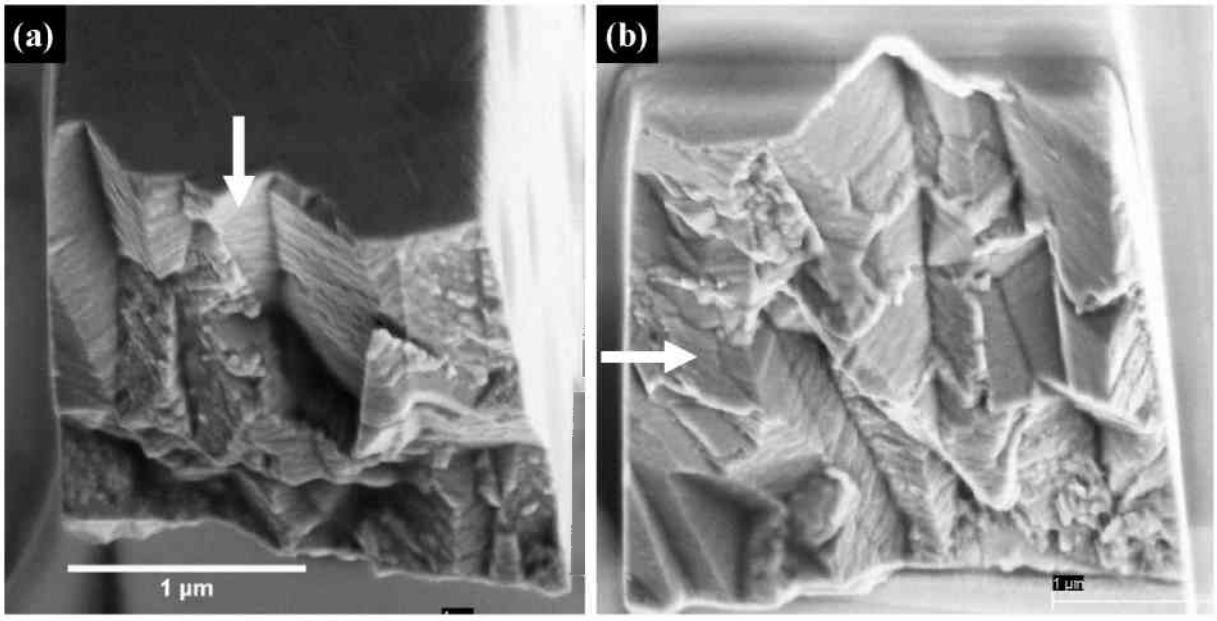

Figure 41. Fracture surface of un-notched $Ti_{0.2}Al_{0.8}N$ cantilevers tested in out-of-plane (a) and in-plane (b) geometries with arrows indicating the loading directions.

5.2.3 Fracture Stress of $Ti_{1-x}Al_xN$ nacre Coating

Compared to the results from the $Ti_{0.2}Al_{0.8}N$ coating and the $Ti_{0.05}Al_{0.95}N$ coating, the $Ti_{1-x}Al_xN$ nacre coating exhibits the highest fracture strength of 6.3 and 7.9 GPa for the in-plane and out-of-plane testing orientations, respectively. The higher value for the out-of-plane orientation could be explained by the successive alternation of two materials with particular elastic properties. As already discussed by Koledník *et. al.*, when a continuous material is periodically interrupted by small regions of elastically softer material, the fracture toughness will increase while at the same time only a small portion of stiffness is lost. This effect observed also in a variety of natural materials (Figure 1) originates from crack trapping at the interfaces [48].

This explanation does not apply obviously apply the in-plane testing geometry, because of the orientation of the interlayers. The softer interlayers cannot work as a crack trap, since the interfaces are oriented parallel to the loading direction, as it is shown schematically in Figure 37.

The fracture surfaces shown Figure 42 indicate that the self-organized crystallites are smaller compared to the crystallites from $Ti_{0.2}Al_{0.8}N$ coating (Figure 41), due to the limited sublayer thicknesses. This is in agreement with the coating microstructure presented in Figure 4 and Figure 27. The fracture surfaces show substantial roughness for both orientations. This indicates that there is a crack deflection present during the fracture process, which can also be used to explain the outstanding fracture strength observed.

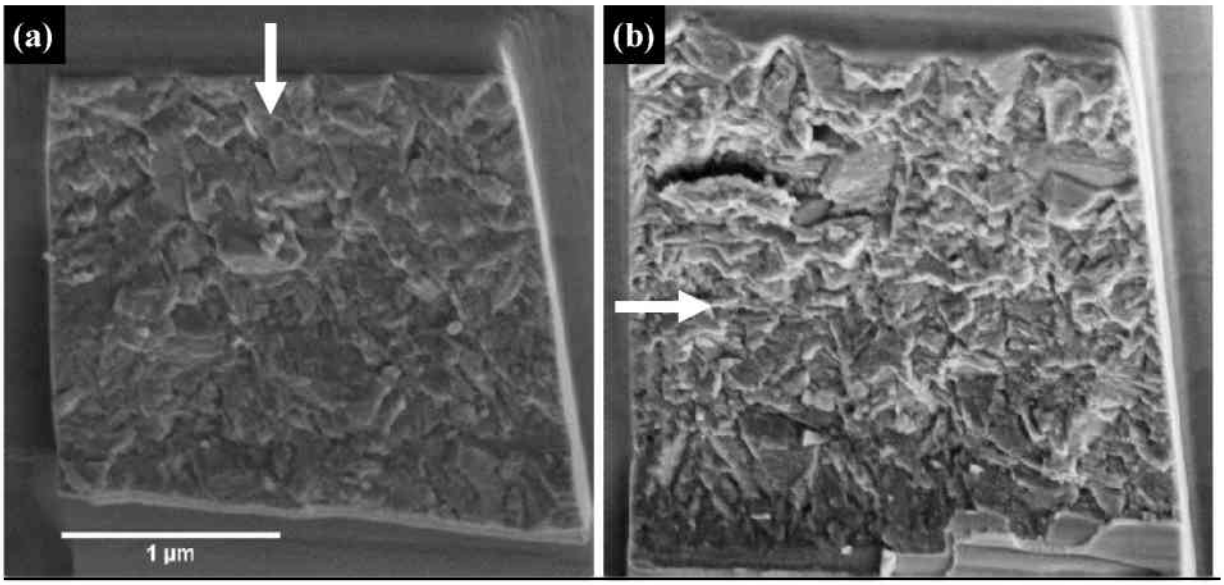

Figure 42. Fracture surface of un-notched $Ti_{1-x}Al_xN$ nacre cantilevers tested in out-of-plane (a) and in-plane (b) geometry with arrows indicating the loading directions.

5.3 Fracture Toughness

In this section the obtained fracture toughness values are discussed and compared for each of the $Ti_{1-x}Al_xN$ coatings, beginning with the $Ti_{0.05}Al_{0.95}N$ coating and followed by the $Ti_{0.2}Al_{0.8}N$ coating and the $Ti_{1-x}Al_xN$ nacre coating.

5.3.1 Fracture Toughness of $Ti_{0.05}Al_{0.95}N$ Coating

The fracture toughness of the $Ti_{0.05}Al_{0.95}N$ coating was evaluated to be 3.1 $MPam^{½}$ both for in-plane and out-of-plane orientation. This is in good agreement with the observed Young's modulus and fracture stress, which also showed no anisotropy (Table 2).

This is also confirmed by the fracture surfaces of the notched cantilevers (cf. Figure 43), which reveal a microstructure comparable to the one observed for the $Ti_{0.05}Al_{0.95}N$ coating (cf. Figure 23) and to the fracture surfaces of the un-notched cantilevers presented (cf. Figure 40). It is again confirmed, that the self-organized crystallites are randomly distributed in a matrix of $Ti_{1-x}Al_xN$ solid solution nanocrystals.

In addition, Figure 43 shows that fracture occurs between these self-organized crystallites. One consequence of the rather small crystallite size is, that there is no pronounced crack deflection along the interfaces, there is no significant barrier for the crack movement in the coating.

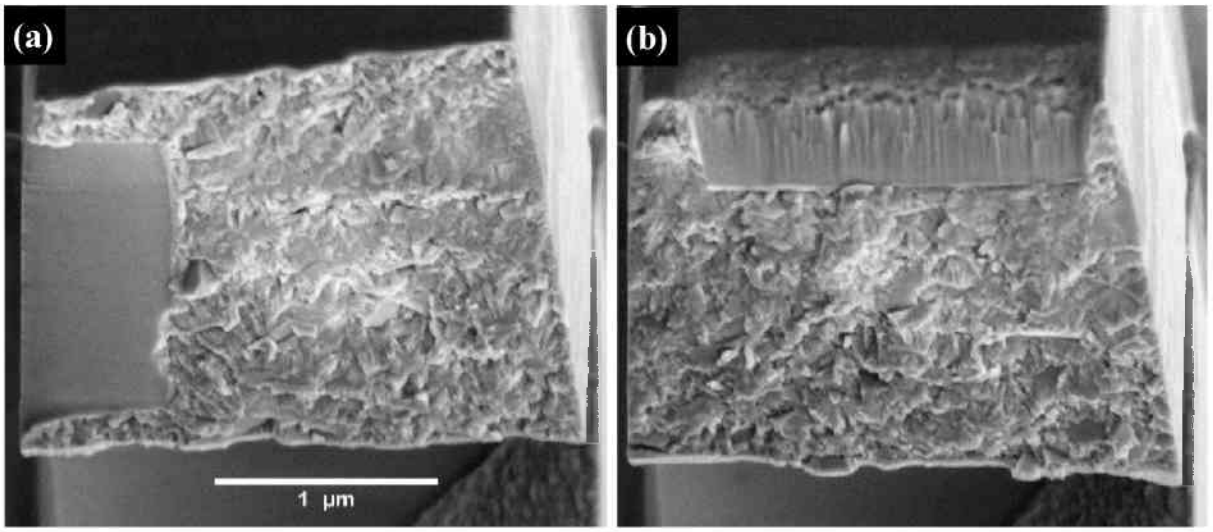

Figure 43. Fracture surface of notched $Ti_{0.05}Al_{0.95}N$ cantilevers tested in in-plane (a) and out-of-plane (b) geometries.

The strain energy release rate G_{Ic} is another measure for the energy needed to move a crack through the material[45]. It is defined as

$$G_{Ic} = \frac{K_{Ic}^2}{E}. \tag{58}$$

The evaluated facture toughness and Young's modulus result in a strain energy release rate for the $Ti_{0.05}Al_{0.95}N$ coating of 42.3 Jm^{-2}.

5.3.2 Fracture Toughness of the $Ti_{0.2}Al_{0.8}N$ Coating

The fracture toughness's for the $Ti_{0.2}Al_{0.8}N$ coating are 5.0 $MPam^{½}$ and 5.4 $MPam^{½}$ for out-of-plane and in-plane orientation, respectively. These relatively high values can be attributed to the unique microstructure of the coatings, which has already been shown in Figure 25 and Figure 41.

This is also confirmed by the fracture surfaces shown in Figure 44. The crack moves along the interfaces between the self-organized crystallites, which leads to a distinct crack deflection from the straight path through the bending cantilever. There is a slight anisotropy in fracture toughness found for in-plane and out-of-plane orientations. The results are supported by the morphology of fracture surfaces, where for in-plane orientation (Figure 44 a) a more pronounced crack deflection is observed, than for the out-of-plane orientation (Figure 44 b).

It can be inferred from Figure 3 and Figure 25 that the microstructure is the result of competitive grain growth, whereby the crystallites grow one into other as it is also shown for two crystallites in Figure 44 a. Consequently, a multiple crack deflection occurs during fracture process, which results in the outstanding fracture toughness.

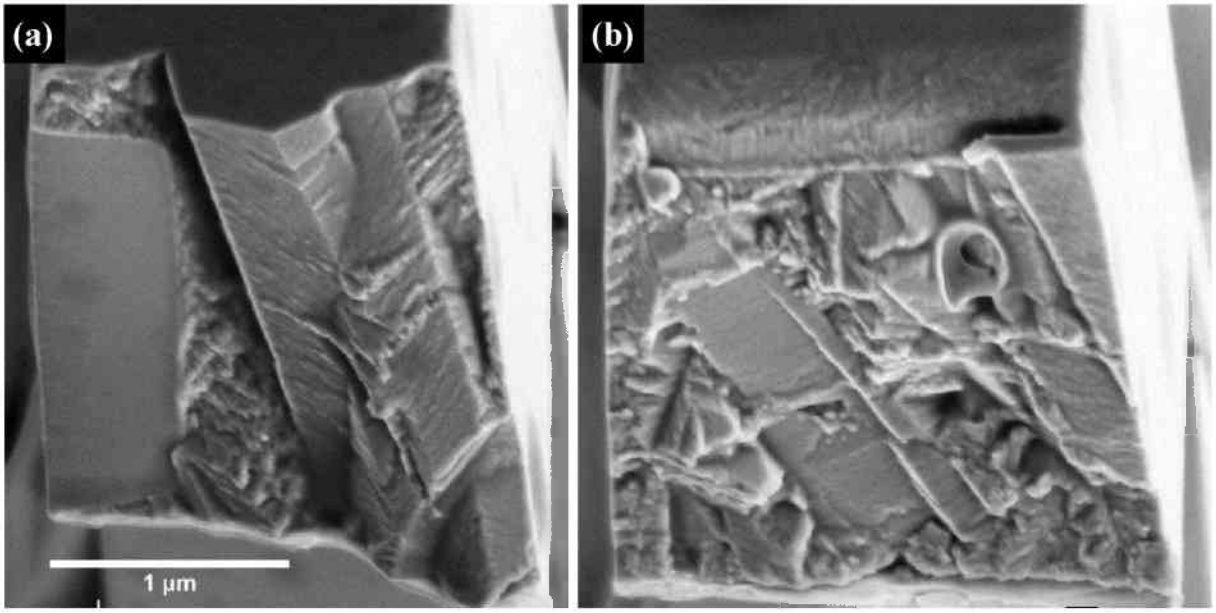

Figure 44. Fracture surface of notched $Ti_{0.2}Al_{0.8}N$ cantilevers tested in in-plane (a) and out-of-plane (b) geometries.

The strain energy release rate was separately evaluated for in-plane and out-of-plane testing orientation, which resulted in 72.9 Jm^{-2} and 64.1 Jm^{-2} respectively.

This means, that the fracture toughness is not only raised by the difference in Young's modulus between the wurtzite and the fcc AlN phase, but also the energy required for the crack growth through the material is raised by at least 50 %. This results is also a consequence of the highly deflected crack path.

5.3.3 Fracture Toughness of the $Ti_{1-x}Al_xN$ nacre Coating

Although the multi-layered $Ti_{1-x}Al_xN$ nacre coating exhibits higher fracture strength, its fracture toughness is below the fracture toughness observed in the $Ti_{0.2}Al_{0.8}N$ coating.

As it was already shown in the STEM micrograph in Figure 27, the growth of the self-organized purely cubic $Ti_{1-x}Al_xN$ sublayers was interrupted by thin layers of cubic-wurtzite $Ti_{1-x}Al_xN$ sublayers, which resulted in a smaller crystallite size than that found in the cubic $Ti_{0.2}Al_{0.8}N$ coating. Therefore the crack deflection was not as pronounced as in the purely cubic $Ti_{0.2}Al_{0.8}N$ coating. This resulted in lower fracture toughness values of 4.2 $MPam^{½}$ and 4.7 $MPam^{½}$ for the in-plane and out-of-plane orientations, respectively.

The observed fracture behaviour is also confirmed by the fracture surfaces of the notched cantilevers in Figure 45, in a good agreement with the microstructure shown in Figure 27 and the fracture surfaces of the un-notched cantilevers from in Figure 42.

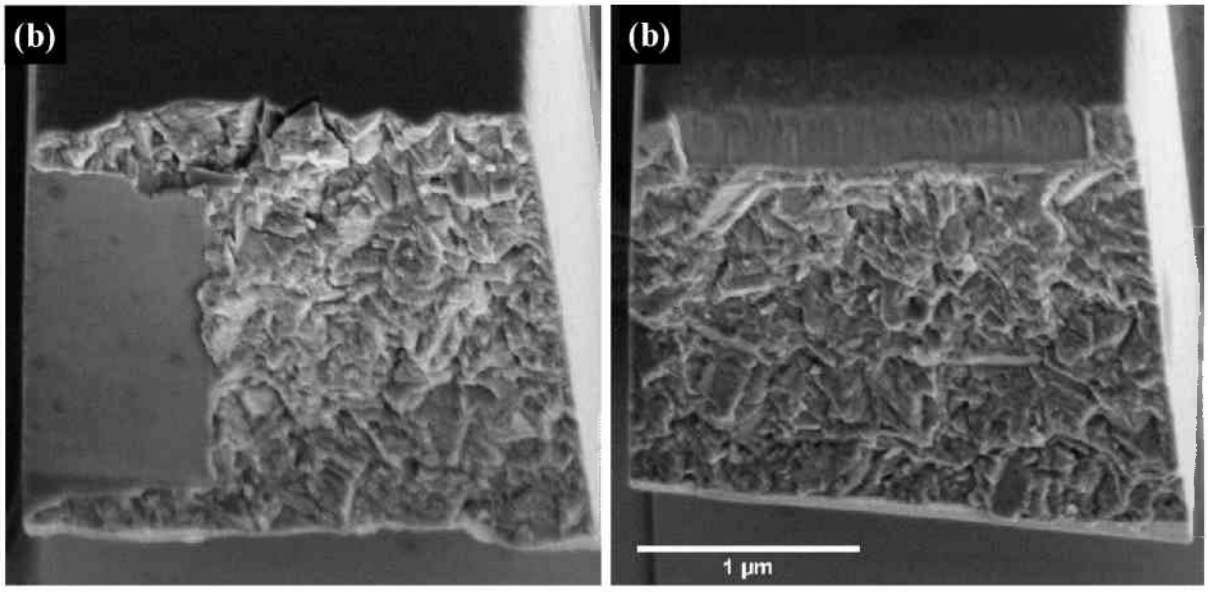

Figure 45. Fracture surface of notched $Ti_{1-x}Al_xN$ nacre cantilevers tested in in-plane (a) and out-of-plane (b) geometries.

The strain energy release rate of 62.2Jm^{-2} and 45.8 Jm^{-2} was evaluated separately for out-of-plane and in-plane testing orientations, respectively. This difference in the strain energy release rate shows, (i) that for the out-of-plane orientation values almost as high as in the $Ti_{0.2}Al_{0.8}N$ coating are achieved, and (ii) that for the in-plane orientation a significant drawback of the strain energy release rate, and therefore fracture toughness exists. It can be therefore concluded, that for the in-plane testing geometry, the $Ti_{0.05}Al_{0.95}N$ interlayers work as weakening component of the material.

6. Conclusions and Further Outlook

The cubic-hexagonal $Ti_{0.05}Al_{0.95}N$ coating revealed good mechanical properties, corresponding with the outstanding oxidation resistance, as it was already reported by Todt et. al. in 2014 [24]. The fracture toughness exceeds those of the previously investigated coatings and coating systems [11][14][41][49]

The cubic-cubic $Ti_{0.2}Al_{0.8}N$ coating exhibited excellent elastic and fracture properties, beginning with Young's modulus up to 400GPa and a fracture stress up to 5.7 GPa. The fracture toughness up to 5.4 $MPam^{½}$ is the most outstanding property of this coating. Together with the good oxidation resistance reported by Todt et. al. in 2016 [25], this coating is very promising for industrial applications.

Even though the new developed $Ti_{1-x}Al_xN$ nacre coating exhibits the highest fracture stress, the corresponding fracture toughness is unfortunately smaller. This can be attributed to the less pronounced crack deflection mechanism predetermined by the grain microstructure and morphology of the $Ti_{1-x}Al_xN$ nacre coating compared to the $Ti_{0.2}Al_{0.8}N$ coating. Further optimization of the nacre microstructure is therefore required in order to optimize the fracture toughness.

7. Acknowledgment

This work would not have been possible without the support of others. A few of them I want to mention here and also express my thanks to them:

- my supervisor Jozef Keckes, for providing me with this interesting topic, for his advices, his encouragement and for his critical review on my work,
- Jakub Zalesak, for supporting me with the STEM-micrographs, and for always have an ear for my problems and questions,
- Juraj Todt and David Gruber for the fruitful discussions in the office,
- Bernhard Sartory and the MCL for the FIB-preparation of the cantilevers tested in this work,
- My parents, Gabriele and Erwin Meindlhumer for supporting me during my studies,

and also I have to express my thanks to many more, which are not mentioned here.

8. References

[1] I. Endler, M. Höhn, M. Herrmann, H. Holzschuh, R. Pitonak, S. Ruppi, H. van den Berg, H. Westphal, and L. Wilde, "Aluminum-rich TiAlCN coatings by Low Pressure CVD," *Surf. Coatings Technol.*, vol. 205, no. 5, pp. 1307–1312, 2010.

[2] I. Endler, M. Höhn, M. Herrmann, R. Pitonak, S. Ruppi, M. Schneider, H. van den Berg, and H. Westphal, "Novel aluminum-rich Ti1 - xAlxN coatings by LPCVD," *Surf. Coatings Technol.*, vol. 203, no. 5–7, pp. 530–533, 2008.

[3] W. Chen, Y. Lin, J. Zheng, S. Zhang, S. Liu, and S. C. Kwon, "Preparation and characterization of CrAlN/TiAlSiN nano-multilayers by cathodic vacuum arc," *Surf. Coatings Technol.*, vol. 265, pp. 205–211, 2015.

[4] P. C. Jindal, A. T. Santhanam, U. Schleinkofer, and A. F. Shuster, "Performance of PVD TiN, TiCN, and TiAlN coated cemented carbide tools in turning," *Int. J. Refract. Met. Hard Mater.*, vol. 17, no. 1, pp. 163–170, 1999.

[5] A. Matthews and A. R. Lefkow, "Problems in the physical vapour deposition of titanium nitride," *Thin Solid Films*, vol. 126, no. 3–4, pp. 283–291, Apr. 1985.

[6] W.-D. Münz, "Titanium aluminum nitride films: A new alternative to TiN coatings," *J. Vac. Sci. Technol. A Vacuum, Surfaces, Film.*, vol. 4, no. 6, p. 2717, 1986.

[7] H. A. Jehn, J.-H. Kim, and S. Hofmann, "Composition and properties of transition metal nitride thin films (ZrNx, NbNx, MoNx)," *Surf. Coatings Technol.*, vol. 36, no. 3–4, pp. 715–727, Dec. 1988.

[8] T. Hurkmans, D. B. Lewis, J. S. Brooks, and W.-D. Münz, "Chromium nitride coatings grown by unbalanced magnetron (UBM) and combined arc/unbalanced magnetron (ABS^{TM}) deposition techniques," *Surf. Coatings Technol.*, vol. 86–87, pp. 192–199, Dec. 1996.

[9] A. Riedl, R. Daniel, M. Stefenelli, T. Schöberl, O. Kolednik, C. Mitterer, and J. Keckes, "A novel approach for determining fracture toughness of hard coatings on the micrometer scale," *Scr. Mater.*, vol. 67, no. 7–8, pp. 708–711, Oct. 2012.

[10] K. Matoy, H. Schönherr, T. Detzel, T. Schöberl, R. Pippan, C. Motz, and G. Dehm, "A comparative micro-cantilever study of the mechanical behavior of silicon based passivation films," *Thin Solid Films*, vol. 518, no. 1, pp. 247–256, Nov. 2009.

[11] S. Massl, W. Thomma, J. Keckes, and R. Pippan, "Investigation of fracture properties of magnetron-sputtered TiN films by means of a FIB-based cantilever bending technique," *Acta Mater.*, vol. 57, no. 6, pp. 1768–1776, Apr. 2009.

[12] A. E. Santana, A. Karimi, V. H. Derflinger, and A. Schütze, "Microstructure and mechanical behavior of TiAlCrN multilayer thin films," *Surf. Coat. Technol.*, vol. 177–178, pp. 334–340, 2004.

[13] V. H. H. Derflinger, A. Schutze, M. Ante, a. Schütze, and M. Ante, "Mechanical and structural properties of various alloyed TiAlN-based hard coatings," *Surf. Coat. Technol.*, vol. 200, no. 16–17, pp. 4693–4700, 2006.

[14] O. Nakonechna, T. Cselle, M. Morstein, and A. Karimi, "On the behaviour of indentation fracture in TiAlSiN hard thin films," *Thin Solid Films*, vol. 447–448, no. 1, pp. 406–412, 2004.

[15] N. Ghafoor, I. Petrov, D. O. Klenov, B. Freitag, J. Jensen, J. E. Greene, L. Hultman, and M. Odén, "Self-organized anisotropic (Zr1−xSix)Ny nanocomposites grown by reactive sputter deposition," *Acta Mater.*, vol. 82, pp. 179–189, 2015.

[16] M. Schlögl, J. Paulitsch, J. Keckes, and P. H. Mayrhofer, "Influence of AlN layers on mechanical properties and thermal stability of Cr-based nitride coatings," *Thin Solid Films*, vol. 531, pp. 113–118, 2013.

[17] J. Lin, J. J. Moore, B. Mishra, M. Pinkas, and W. D. Sproul, "Nano-structured CrN/AlN multilayer coatings synthesized by pulsed closed field unbalanced magnetron sputtering," *Surf. Coatings Technol.*, vol. 204, no. 6–7, pp. 936–940, 2009.

[18] P. Yi, L. Peng, and J. Huang, "Multilayered TiAlN films on Ti6Al4V alloy for biomedical applications by closed field unbalanced magnetron sputter ion plating process," *Mater. Sci. Eng. C*, vol. 59, pp. 669–676, 2016.

[19] M. Schlögl, C. Kirchlechner, J. Paulitsch, J. Keckes, and P. H. Mayrhofer, "Effects of structure and interfaces on fracture toughness of CrN/AlN multilayer coatings," *Scr. Mater.*, vol. 68, no. 12, pp. 917–920, 2013.

[20] Y. Tanaka, T. M. Gür, M. Kelly, S. B. Hagstrom, T. Ikeda, K. Wakihira, and H. Satoh, "Properties of (Ti1−xAlx)N coatings for cutting tools prepared by the cathodic arc ion plating method," *J. Vac. Sci. Technol. A Vacuum, Surfaces, Film.*, vol. 10, no. 4, p. 1749, 1992.

[21] N. E. Cristensen and I. Gorczyca, "Calculated structural phase transitions of aluminium nitride under pressure," *Phys. Rev. B*, vol. 47, no. 8, pp. 4307–4314, 1992.

[22] R. F. Zhang and S. Veprek, "Metastable phases and spinodal decomposition in Ti1-xAlxN system studied by ab initio and thermodynamic modeling, a comparison with the TiN-Si3N4 system," *Mater. Sci. Eng. A*, vol. 448, no. 1–2, pp. 111–119, 2007.

[23] L. Zhang, H. Yang, X. Pang, K. Gao, and A. A. Volinsky, "Microstructure, residual stress, and fracture of sputtered TiN films," *Surf. Coatings Technol.*, vol. 224, pp. 120–125, Jun. 2013.

[24] J. Todt, R. Pitonak, a. Köpf, R. Weißenbacher, B. Sartory, M. Burghammer, R. Daniel, T. Schöberl, and J. Keckes, "Superior oxidation resistance, mechanical properties and residual stresses of an Al-rich nanolamellar Ti0.05Al0.95N coating prepared by CVD," *Surf. Coatings Technol.*, vol. 258, pp. 1119–1127, 2014.

[25] J. Todt, J. Zalesak, R. Daniel, R. Pitonak, A. Köpf, R. Weißenbacher, B. Sartory, C. Mitterer, and J. Keckes, "Al-rich cubic Al0.8Ti0.2N coating with self-organized nano-lamellar microstructure: Thermal and mechanical properties," *Surf. Coatings Technol.*, vol. 291, pp. 89–93, 2016.

[26] E. Arzt, "Biological and artificial attachment devices: Lessons for materials scientists from flies and geckos," *Mater. Sci. Eng. C*, vol. 26, no. 8, pp. 1245–1250, 2006.

[27] M. A. Meyers, J. McKittrick, and P. Y. Chen, "Structural biological materials: critical mechanics-materials connections," *Science*, vol. 339, no. 6121, pp. 773–779, 2013.

[28] F. Barthelat and H. D. Espinosa, "An experimental investigation of deformation and fracture of nacre-mother of pearl," *Exp. Mech.*, vol. 47, no. 3, pp. 311–324, 2007.

[29] F. Barthelat, Z. Yin, and M. J. Buehler, "Structure and mechanics of interfaces in biological materials," *Nat. Rev. Mater.*, p. 16007, 2016.

[30] F. Barthelat, H. Tang, P. D. Zavattieri, C. M. Li, and H. D. Espinosa, "On the mechanics of mother-of-pearl: A key feature in the material hierarchical structure," *J. Mech. Phys. Solids*, vol. 55, no. 2, pp. 306–337, 2007.

[31] M. Sarikaya, K. E. Gunnison, M. Yasrebi, and I. A. Aksay, "Mechanical Property-Microstructural Relationships in Abalone Shell," *Mater. Reseaerch Soc. Symp.*, vol. 174, pp. 109–116, 1990.

[32] M. Stefenelli, R. Daniel, W. Ecker, D. Kiener, J. Todt, A. Zeilinger, C. Mitterer, M. Burghammer, and J. Keckes, "X-ray nanodiffraction reveals stress distribution across an indented multilayered CrN–Cr thin film," *Acta Mater.*, vol. 85, pp. 24–31, Feb. 2015.

[33] P. J. Imrich, C. Kirchlechner, D. Kiener, and G. Dehm, "Internal and external stresses: In situ TEM compression of Cu bicrystals containing a twin boundary," *Scr. Mater.*, vol. 100, pp. 94–97, 2015.

[34] D. KIENER, R. PIPPAN, C. MOTZ, and H. KREUZER, "Microstructural evolution of the deformed volume beneath microindents in tungsten and copper," *Acta Mater.*, vol. 54, no. 10, pp. 2801–2811, Jun. 2006.

[35] J. Zalesak, M. Bartosik, R. Daniel, C. Mitterer, C. Krywka, D. Kiener, P. H. Mayrhofer, and J. Keckes, "Cross-sectional structure-property relationship in a graded nanocrystalline Ti<inf>1-x</inf>Al<inf>x</inf>N thin film," *Acta Mater.*, vol. 102, pp. 212–219, 2016.

[36] K. Matoy, H. Schönherr, T. Detzel, and G. Dehm, "Micron-sized fracture experiments on amorphous SiOx films and SiOx/SiNx multi-layers," *Thin Solid Films*, vol. 518, no. 20, pp. 5796–5801, Aug. 2010.

[37] M. W. Kapp, A. Hohenwarter, S. Wurster, B. Yang, and R. Pippan, "Anisotropic deformation characteristics of an ultrafine- and nanolamellar pearlitic steel," *Acta Mater.*, vol. 106, pp. 239–248, Mar. 2016.

[38] S. Wurster, C. Motz, and R. Pippan, "Characterization of the fracture toughness of micro-sized tungsten single crystal notched specimens," *Philos. Mag.*, vol. 92, no. 14, pp. 1803–1825, May 2012.

[39] P. J. Imrich, C. Kirchlechner, C. Motz, and G. Dehm, "Differences in deformation behavior of bicrystalline Cu micropillars containing a twin boundary or a large-angle grain boundary," *Acta Mater.*, vol. 73, pp. 240–250, Jul. 2014.

[40] Y. X. Wang, S. Zhang, J. W. Lee, W. S. Lew, and B. Li, "Influence of bias voltage on the hardness and toughness of CrAlN coatings via magnetron sputtering," *Surf. Coatings Technol.*, vol. 206, no. 24, pp. 5103–5107, 2012.

[41] Q. Wang, F. Zhou, and J. Yan, "Evaluating mechanical properties and crack resistance of CrN, CrTiN, CrAlN and CrTiAlN coatings by nanoindentation and scratch tests," *Surf. Coatings Technol.*, vol. 285, pp. 203–213, 2016.

[42] W. C. Oliver and G. M. Pharr, "An improved technique for determining hardness and elastic modulus using load and displacement sensing indentation experiments," *J. Mater. Res.*, vol. 7, no. 06, pp. 1564–1583, 1992.

[43] F. Ziegler, *Technische Mechanik der festen und flüssigen Körper*. 1992.

[44] E. Carrera, G. Giunta, and M. Petrolo, *Beam Structures Classical and Advanced Theories*. 2011.

[45] D. Gross and T. Seelig, *Bruchmechanik Mit einer Einführung in die Mikromechanik*, 4th ed. 2006.

[46] H. Tada, P. C. Paris, and G. R. Irwin, *The Stress Analysis of Cracks Handbook*, 3rd ed. New York, 2000.

[47] W. C. Oliver and G. M. Pharr, "Measurement of hardness and elastic modulus by instrumented indentation: Advances in understanding and refinements to methodology," *J. Mater. Res.*, vol. 19, no. 01, pp. 3–20, 2004.

[48] O. Kolednik, J. Predan, F. D. Fischer, and P. Fratzl, "Bioinspired Design Criteria for Damage-Resistant Materials with Periodically Varying Microstructure," *Adv. Funct. Mater.*, vol. 21, no. 19, pp. 3634–3641, Oct. 2011.

[49] C.-M. Kao, J.-W. Lee, H.-W. Chen, Y.-C. Chan, J.-G. Duh, and S.-P. Chen, "Microstructures and mechanical properties evaluation of TiAlN/CrSiN multilayered thin films with different bilayer periods," *Surf. Coatings Technol.*, vol. 205, no. 5, pp. 1438–1443, 2010.

9. Index of Figures

10. Index of Tables